AD-A094 189 WASHINGTON UNIV ST LOUIS MO SEMICONDUCTOR RESEARCH LAB F/G 17/5
GALLIUM ARSENIDE WAVEGUIDE DETECTOR ARRAY FOR ELECTRONIC WARFAR--ETC(U)
AUG 80 C M WOLFE, G F SHADE N00014-79-C-0572
UNCLASSIFIED 64382-1 NL

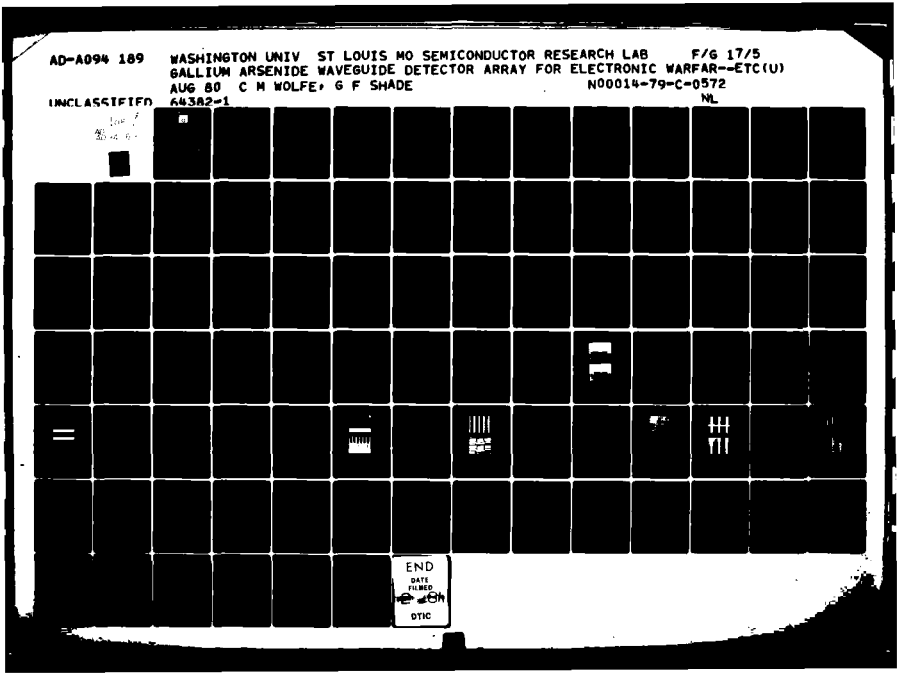

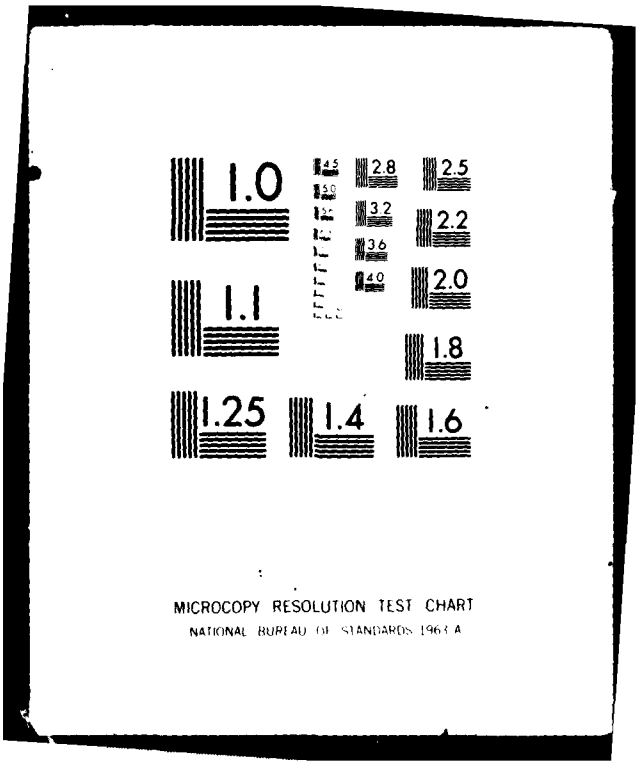
1.0
1.1
1.25
1.4
1.6
1.8
2.0
2.2
2.5
2.8
3.2
3.6
4.0
4.5
5.0
MICROCOPY RESOLUTION TEST CHART
NATIONAL BUREAU OF STANDARDS 1963 A

LEVEL II

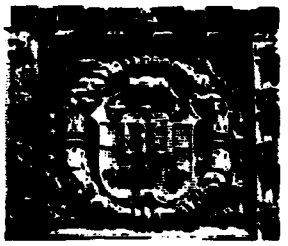

WASHINGTON UNIVERSITY

SCHOOL OF ENGINEERING AND APPLIED SCIENCE

AD A094189

DDC FILE COPY

FINAL TECHNICAL REPORT
No. 64382-1

GALLIUM ARSENIDE WAVEGUIDE DETECTOR ARRAY
FOR ELECTRONIC WARFARE SUPPORT
MEASURE SYSTEMS

29 August 1980
By
Semiconductor Research Laboratory
Box 1127
Washington University
Saint Louis, Missouri 63130
For
Naval Research Laboratory
Code 5262
Washington, DC 20375

Contract No. N00014-79-C-0572

1 July 1979 to 30 June 1980

Approved for public release;
distribution unlimited

DTIC
ELECTE
JAN 27 1981
S
C

WASHINGTON UNIVERSITY / ST.

81 1 26 205

Unclassified

SECURITY CLASSIFICATION OF THIS PAGE (When Data Entered)

REPORT DOCUMENTATION PAGE	READ INSTRUCTIONS BEFORE COMPLETING FORM
1. REPORT NUMBER	2. GOVT ACCESSION NO. AD-A094 189
3. RECIPIENT'S CATALOG NUMBER (9) Final Report	
4. TITLE (and Subtitle) (6) Gallium Arsenide Waveguide Detector Array for Electronic Warfare Support Measure Systems	5. TYPE OF REPORT & PERIOD COVERED (14) 1 [illegible] 79-30 Jun 80
	6. PERFORMING ORG. REPORT NUMBER 64382-1
7. AUTHOR(s) (10) C.M. Wolfe G.F. Shade	8. CONTRACT OR GRANT NUMBER(s) (15) N00014-79-C-0572
9. PERFORMING ORGANIZATION NAME AND ADDRESS Semiconductor Research Laboratory Box 1127 Washington University St. Louis, MO 63130	10. PROGRAM ELEMENT, PROJECT, TASK AREA & WORK UNIT NUMBERS
11. CONTROLLING OFFICE NAME AND ADDRESS (11) Naval Research Laboratory Code 5262 Washington, DC 20375	12. REPORT DATE 29 August 1980
	13. NUMBER OF PAGES 83
14. MONITORING AGENCY NAME & ADDRESS (if different from Controlling Office) (12) 88	15. SECURITY CLASS. (of this report) Unclassified
	15a. DECLASSIFICATION/DOWNGRADING SCHEDULE

16. DISTRIBUTION STATEMENT (of this Report)

The United States Government is authorized to reproduce and distribute this report for Governmental purposes.

17. DISTRIBUTION STATEMENT (of the abstract entered in Block 20, if different from Report)

18. SUPPLEMENTARY NOTES

19. KEY WORDS (Continue on reverse side if necessary and identify by block number)

GaAs, photodiode array, integrated optical circuit

20. ABSTRACT (Continue on reverse side if necessary and identify by block number)

This report presents the results from a study of a waveguide detector array implemented on GaAs. Each component of the array is developed to provide a model for determining the array operation. The fabrication procedures are then discussed in some detail. Each process step is described and the results evaluated.

The finished array is then tested. Several measurements are made to determine the response characteristics, dynamic range,

DD FORM 1 JAN 73 1473 EDITION OF 1 NOV 65 IS OBSOLETE

Unclassified

SECURITY CLASSIFICATION OF THIS PAGE (When Data Entered)

411361

20. Abstract (Continued)

crosstalk, and device uniformity. The results of these measurements are then analyzed and comments made on the potential uses of this device.

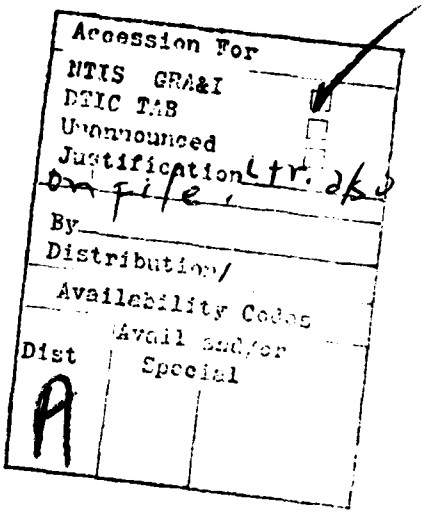

TABLE OF CONTENTS

TABLE OF CONTENTS
(continued)

1. INTRODUCTION

Integrated optical circuits (IOCs) combining optical signal propagation with high speed photoelectric detection have a high potential for very fast analog and digital signal processing. Gallium arsenide shows considerable promise as a semiconductor for use in IOC fabrication because of the variety of available optical and electronic device technologies for this material. Along with these technologies is the potential for optical signal generation, propagation, and detection on a single substrate. This provides the key to the design of a monolithic IOC for real-time, wide bandwidth spectrum analysis. One of the basic elements for an integrated spectrum analyzer is the waveguide detector array. The properties of this component will determine the ultimate capabilities of the IOC spectrum analyzer.

1.1 GaAs-BASED IOCs

Gallium arsenide has good potential for the fabrication of IOCs. A large variety of electronic and optical devices have been demonstrated in GaAs with the desirable attributes of high speed, low noise, and high efficiency. Lindley *et al* [1] have fabricated avalanche photodetectors with a large gain-bandwidth product(less than 50 GHz) and a signal-to-noise ratio of 30 dB. Stillman *et al* [2]

* The numbers in parentheses in the text indicate references in the Bibliography.

have fabricated GaAs waveguides which operate with attenuation as low as 2 cm^{-1} at GaAs laser wavelengths. In addition, GaAs-AlGaAs double heterostructure lasers emitting at 9100 Å have been integrated with high purity GaAs waveguides [3]. Sun *et al* [4] have utilized GaAs waveguide detectors to achieve time demultiplexing at data rates of 1 Mbps. These electroabsorption avalanche photodiode (EAP) detectors make use of the Franz-Keldysh effect to detect optical radiation at wavelengths beyond the normal absorption edge of GaAs [4-7]. Their use as an output stage provides the key to monolithic integration of optical circuits in GaAs; that is, with EAP devices, signal generation, propagation, processing, and optoelectronic decoding are possible on a single substrate.

1.2 GaAs IOC SPECTRUM ANALYZER

One application for such a monolithic IOC is real time, wide bandwidth spectrum analysis. A hypothetical configuration for an integrated GaAs spectrum analyzer is shown in Figure 1. To provide the coherent optical beam a distributed feedback, distributed Bragg reflector, or integrated Fabry-Perot laser is used. This beam is then RF modulated with either an acousto-optical or electro-optical transducer. The encoded signal is then Fourier transformed with a Fresnel or Luneberg lens.

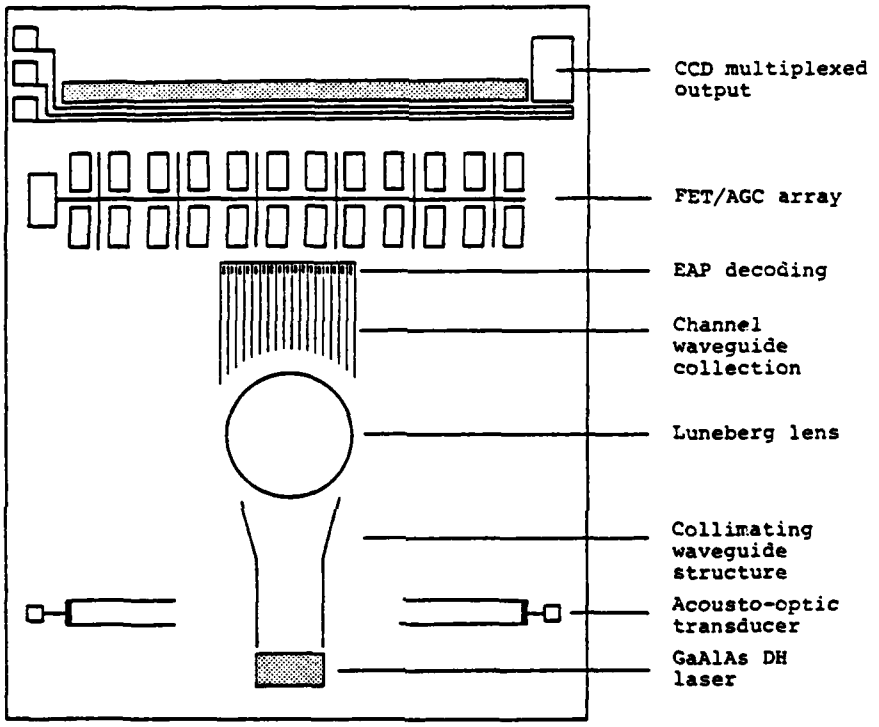

Figure 1 Schematic of a hypothetical GaAs IOC for real-time spectrum analysis.

The resulting signal spectrum is collected by an array of integrated channel waveguides terminated in EAP detectors. These detectors convert the optical information into a compatible electrical signal. The resulting signal can then be processed with charge coupled devices (CCDs) for the final output. Such an IOC spectrum analyzer has been examined by Anderson *et al* [8] on a silicon substrate. They concluded that such a system is a realizable application of present integrated optics technology in silicon. Further investigation and experimental development are necessary, however, to assure optimum design and performance.

1.3 WAVEGUIDE DETECTOR ARRAY

One of the basic elements for a wide bandwidth spectrum analyzer is the waveguide detector array. Discrete GaAs avalanche photodiodes [1] have been found to have a higher gain-bandwidth product and an enhanced signal-to-noise ratio (30dB), as compared to silicon devices, because of the higher ratio of the hole to electron ionization coefficients in GaAs [9]. In the electroabsorption avalanche photodiode (EAP) mode of operation [4,7], these devices are capable of detecting the below bandgap GaAs laser emission with a measured response time of less than one nanosecond [7]. Results for GaAs EAP devices in waveguide configuration are equivalent to those for discrete detectors [4]. Since

both the gain and absorption are controlled by the bias, GaAs EAP devices have a useful dynamic range which is orders of magnitude larger than silicon devices where only the gain is controlled by the bias. For these reasons, an array of GaAs EAP detectors in waveguide configuration has been proposed, designed, and fabricated with monolithic FET automatic response control.

1.4 CIRCUIT APPLICATION

The desired waveguide detector array should provide high speed detection of GaAs laser emission over a large incident power range. The circuit for obtaining this result should be composed of GaAs components that can be integrated on a single substrate. To meet these requirements, the circuit shown in Figure 2 has been chosen. With this circuit, high speed detection is possible while also providing automatic response control. The benefit of the automatic response control is two-fold. First, the input optical power range is extended. Second, the electrical signal output range is compressed. Implementing this circuit on GaAs provides the potential for an integrated waveguide detector array with a high speed of response and a wide dynamic range. In the next section, the operation of this circuit will be considered in detail following the discussions of the individual components.

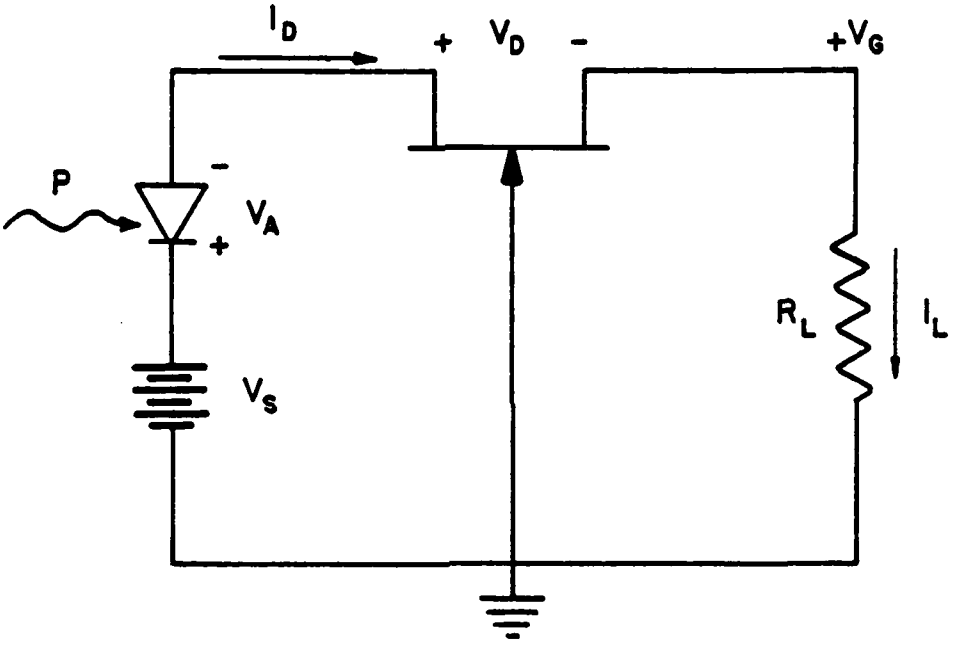

Figure 2 Automatic response control circuit.

2. ANALYSIS

The following analyses will consider each component of the array. For each component, relations will be presented that show its applicability to the array. These relations will then be used to analyze the operation of the automatic response control. The waveguides will be considered first, followed by the detectors and the field effect transistors.

2.1 WAVEGUIDES

The waveguides are etched channel structures as shown in Figure 3. The guiding layer is n-type epitaxial GaAs which is 5 μm thick with a carrier concentration of $10^{15}cm^{-3}$. The supporting layer is also n-type GaAs with a carrier concentration of $10^{18}cm^{-3}$ and a thickness of 30 μm. Both layers are grown on a GaAs semi-insulating substrate by vapor phase epitaxy as will be described in the section on epitaxial growth.

2.1.1 Index of Refraction Difference

The index of refraction of a semiconductor will vary slightly with the carrier concentration of the material due to free carrier absorption. This property can be utilized to obtain changes in the material index whereby optical beam guiding is possible. For the etched channel waveguides of this work, the change in index was provided

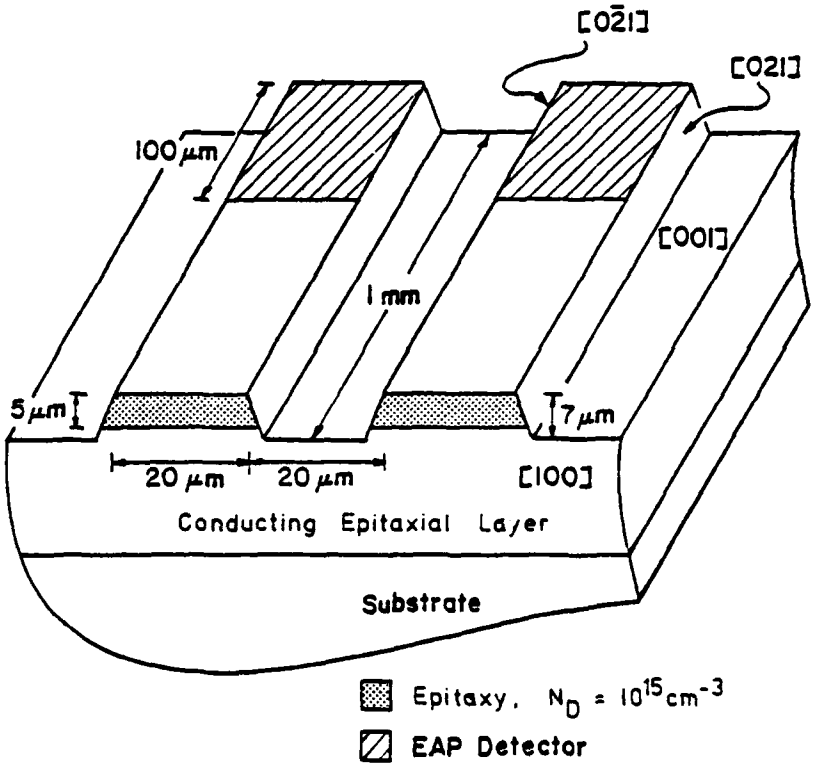

Figure 3 Illustration of the channel waveguide detector structure.

by growing two layers in contact with different doping levels. The amount of this change in index will now be discussed.

From the Kramers-Kronig relations [10], the approximate index of refraction for a semiconductor is,

$$n^2 \simeq \frac{1}{2}(\varepsilon_R - \frac{\sigma_i}{\omega\varepsilon_o}) + \frac{1}{2}\left[(\varepsilon_R - \frac{\sigma_i}{\omega\varepsilon_o})^2 + \frac{\sigma_r^2}{\omega^2\varepsilon_o^2}\right]^{1/2}. \quad (1)$$

The relative permitivity is ε_R. The real and imaginary parts of the high frequency conductivity are σ_r and σ_i, respectively. ω is the frequency of the optical signal. The form of the conductivity components are as follows:

$$\sigma_r = \frac{Nq^2}{m}\left\langle\frac{\tau_m}{1+\omega^2\tau_m^2}\right\rangle, \quad (2a)$$

and

$$\sigma_i = \frac{Nq^2\omega}{m}\left\langle\frac{\tau_m^2}{1+\omega^2\tau_m^2}\right\rangle. \quad (2b)$$

Here N is the doping level, q, the charge of the electron, m, the free electron mass, and τ_m is the momentum relaxation time.

The quantity, $\omega^2\tau_m^2$ is approximately one at microwave frequencies and is much greater than one at optical

frequencies. Therefore, equations (2a) and (2b) reduce to,

$$\sigma_r = \frac{Nq^2}{m\omega^2} \left\langle \frac{1}{\tau_m} \right\rangle, \tag{3a}$$

and

$$\sigma_i = \frac{Nq^2}{m\omega} . \tag{3b}$$

It is then apparent that for optical frequencies, $\sigma_i >> \sigma_r$. So the last term in equation (1) is neglected and the approximation for σ_i, equation (3b) is substitued such that,

$$n^2 = \epsilon_R - \frac{Nq^2}{m\epsilon_o\omega^2} \tag{4}$$

Thus for two semiconductor layers differing only in doping level,

$$n_1^2 - n_2^2 = (N_2 - N_1) \frac{q^2}{m\epsilon_o\omega^2} \tag{5}$$

is the difference in index of refraction. N_1 and N_2 are the doping levels corresponding to the layers of indices n_1 and n_2. Replacing the frequency by the relation,

$$\omega = 2\pi c/\lambda_o$$

one obtains,

$$n_1^2 - n_2^2 = (N_2 - N_1) \frac{q^2\lambda_o^2}{4\pi^2\epsilon_o mc^2} . \tag{6}$$

Applying this equation to the present situation yields a difference in the square of the indices of order 10^{-3}.

2.1.2 Mode Selection

The waveguide structure can be approximated as an asymmetric slab waveguide as shown in Figure 4. This is possible because the operating wavelength inside the guide is much less than the guide width. The solutions presented here are derived by Marcuse [11] and the notation is chosen to be consistent with his results. Both the TE and TM modes will be considered and the eigenvalue equation will be given which determines the number of guided modes. To begin, the following relations are needed.

$$v = \omega/\beta \tag{7}$$

$$k^2 = \omega^2 \varepsilon_o \mu_o = \left(\frac{2\pi}{\lambda_o}\right)^2 \tag{8}$$

and the abbreviations,

$$K = (n_1^2 k^2 - \beta^2)^{1/2} = n_1 k \sin \theta_1 \tag{9a}$$

$$\gamma = (\beta^2 - n_2^2 k^2)^{1/2} = [(n_1^2 - n_2^2)\, k^2 - K^2]^{1/2} \tag{9b}$$

$$\delta = (\beta^2 - n_3^2 k^2)^{1/2} = [(n_1^2 - n_3^2) k^2 - K^2]^{1/2} \tag{9c}$$

The assumption is made that

$$\partial/\partial y = 0$$

with no loss of generality.

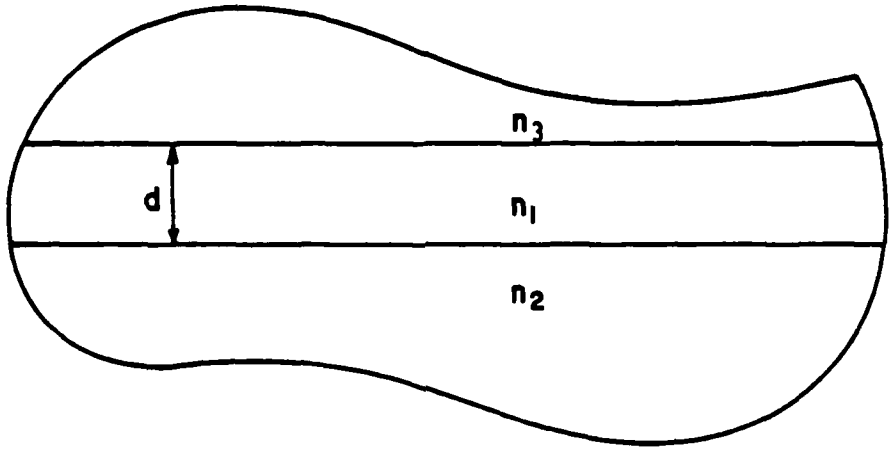

Figure 4 Structure used to derive the mode selection rule for the channel waveguide.

For the guided TE modes the eigenvalue equation obtained is,

$$\tan Kd = K(\gamma + \delta)/(K^2 - \gamma\delta), \tag{10}$$

or alternatively,

$$\cos Kd = \pm (K^2 - \gamma\delta)[(K^2 + \gamma^2)(K^2 + \delta^2)]^{-1/2} \tag{11}$$

$$\sin Kd = \pm K(\gamma + \delta)[(K^2 + \gamma^2)(K^2 + \delta^2)]^{-1/2}, \tag{12}$$

where the sign of the square root must be the same for both.

Cutoff then occurs when,

$$\beta = n_2 k \tag{13a}$$

or,

$$\gamma = 0 . \tag{13b}$$

At this point, it is useful to define a parameter, V, that combines the difference in the squares of the refractive indices n_1, and n_2, with information about the operating wavelength and thickness of the slab waveguide.

$$V = (n_1^2 - n_2^2)^{1/2} kd . \tag{14}$$

The value of V at cutoff can be obtained from equation (10) and for each mode one obtains,

$$V_c = (Kd)_c \tag{15}$$

Then from (9a), (9b), (13a), and (10)

$$V_c = \arctan \left[(n_2^2 - n_3^2)^{1/2} (n_1^2 - n_2^2)\right]^{-1/2} + \nu\pi, \tag{16}$$

where ν is an integer ≥ 0

Similarly, for the TM or transverse magnetic modes, one obtains the eigenvalue equation,

$$\tan Kd = n_1^2 K \, (n_3^2 \, \gamma + n_2^2 \delta) \, (n_2^2 n_3^2 K^2 - n_1^4 \gamma\delta)^{-1}, \tag{17}$$

or,

$$\cos Kd = \pm \, (n_2^2 n_3^2 K^2 - n_1^4 \gamma\delta) \left[(n_2^4 K^2 + n_1^4 \gamma^2) \, (n_3^4 K^2 + n_1^4 \delta^2)\right]^{-1/2}, \tag{18}$$

and,

$$\sin Kd = \pm \, n_1^2 K (n_3^2 \gamma + n_2^2 \delta) \left[(n_2^4 K^2 + n_1^4 \gamma^2) \, (n_3^4 K^2 + n_1^4 \delta^2)\right]^{-1/2}, \tag{19}$$

Again the condition at cutoff is,

$$V_c = (Kd)_c, \tag{20}$$

but now,

$$V_c = \arctan \left\{ \frac{(n_1^2 n_3^{-2}) \quad (n_2^2 - n_3^2)^{1/2}}{(n_1^2 - n_2^2)^{1/2}} \right\} + \nu\pi. \qquad (21)$$

For a given value of V as defined in equation (14) the mode is cut off if $V > V_c$ for that mode. Since $\nu = 0$ indicates the first mode, $\nu = N$ indicates the $(n + 1)$th mode. Thus, for the TE modes,

$$V < N\pi + \arctan \left\{ (n_2^2 - n_3^2)^{1/2} (n_1^2 - n_2^2)^{-1/2} \right\}, \qquad (22)$$

where N is the number of modes below cutoff.
Therefore, the number of modes N is,

$$N = \left(\frac{1}{\pi}\right) V - \arctan \left[\eta (n_2^2 - n_3^2)^{1/2} \quad (n_1^2 - n_2^2)^{1/2} \right]_{int} \qquad (23)$$

where $[\,]_{int}$ indicates the greatest integer less than the value of the brackets plus one and η is

$$\eta = \begin{cases} 1 \text{ for TE modes} \\ n_1^2/n_3^2 \text{ for TM modes.} \end{cases} \qquad (24)$$

The total number of modes is the sum of modes, N, given in equation (23) for both the TE and TM case.

2.2 ELECTROABSORPTION AVALANCHE PHOTODIODES

The photodetector array utilizes electroabsorption avalanche photodiodes (EAPs) to detect the below bandgap emission of GaAs lasers. This is made possible by the

shift in the absorption edge due to high electric fields in the device. This shift is known as the Franz-Keldysh effect. The structure for the EAPs is shown in Figure 5. The avalanche diode is fabricated in waveguide configuration with an aluminum Schottky barrier on a 5 μm thick epitaxial layer of GaAs. The layer thickness is T, and the depletion width for a voltage (-V) is W. The length of the device is L. The parameters N_1, N_2, N_s, and n_1, n_2, n_s are the doping levels and indices of refraction respectively for the waveguide layer, contact layer, and substrate.

2.2.1 Electric Field Distribution

The operation of the EAP detector will be determined by the absorption of the incident radiation and the resulting current. To consider the absorption, the field in the device must be determined. Two cases are possible for the field solutions. In the first, the field is confined to the waveguide layer and W < T. In the second, the depletion depth is approximately equal to the layer thickness.

First consider the case where W < T. Without illumination, the depletion width is W and the depletion approximation holds, so that the electron and hole concentrations are negligible. It is also assumed that the carrier concentration N_1 is approximately equal to the doping

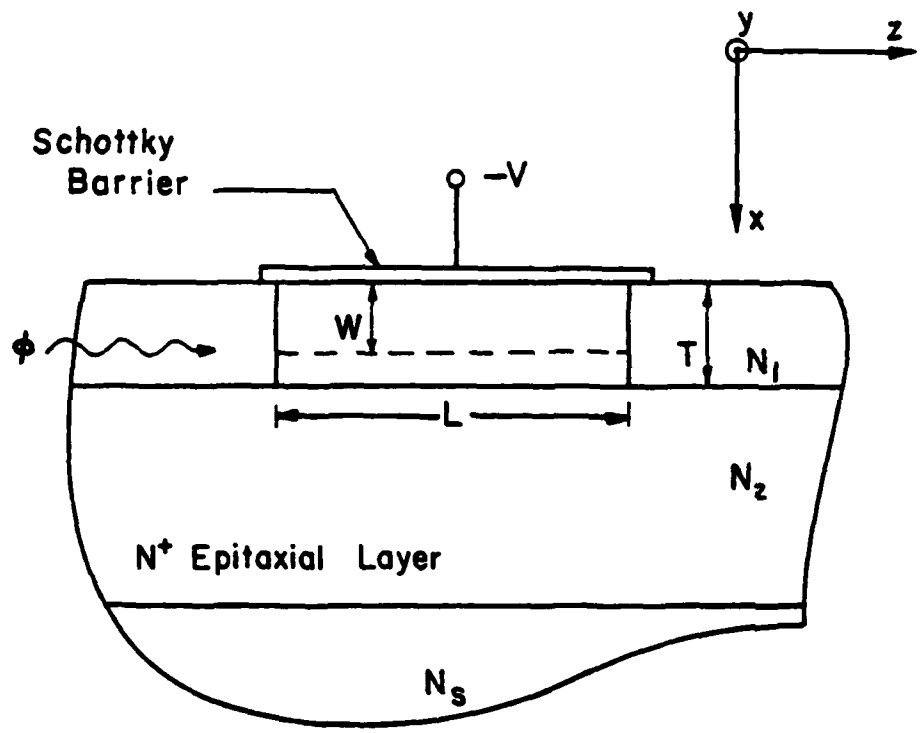

Figure 5 Structure used to derive the EAP operating characteristics.

level N_d. Under these conditions, Poisson's equation can be solved for the field distribution.

$$\frac{dE}{dx} = \frac{q}{\varepsilon} N_1 \tag{25}$$

yielding,

$$E = \frac{q}{\varepsilon} N_1 x + C, \tag{26}$$

The depletion layer is defined as the region of non-zero field. Therefore, at W the field must vanish and,

$$E = \frac{1}{\varepsilon} q N_1 (x-W). \tag{27}$$

Equating the field to the negative derivative of the potential allows a solution for W in terms of V.

$$E = \frac{-d\psi}{dx} = \frac{1}{\varepsilon} q N_1 (x-W) \tag{28}$$

Integrating

$$\psi (x) = \frac{1}{\varepsilon} q N_1 (xW - \frac{x^2}{2}) + C_2 \tag{29}$$

By noting that -V is the potential at x = 0 one obtains,

$$\psi (x) = \frac{1}{\varepsilon} q N_1 (Wx - \frac{x^2}{2}) - V. \tag{30}$$

Substituting the value $\psi (W) = 0$, yields,

$$V = \frac{1}{\varepsilon} qN_1 \frac{W^2}{2} \tag{31}$$

or,

$$W = (\frac{2\varepsilon}{qN_1})^{1/2} V^{1/2}. \tag{32}$$

The final form for the field is then,

$$E(x) = \frac{q}{\varepsilon} N_1 x - \frac{2V}{W}. \tag{33}$$

The case that remains is when the depletion width is equal to or exceeds the layer thickness. For this structure, N_2 is highly doped to be conducting and $N_1 << N_2$ to provide guiding in the layer. Under these conditions the field will not extend very far into the conduction layer and $W \simeq T$, but $E(W) \neq 0$. Again Poisson's equation is integrated to obtain,

$$E(x) = \frac{qN_1}{\varepsilon} x + E(0), \tag{34}$$

and from equation (28),

$$\psi(W) = - T\left[E(0)\right] - \frac{qN_1}{2\varepsilon} T^2 = V. \tag{35}$$

The pinch-off voltage, V_p, is defined as the applied voltage such that the depletion width is T, and $E(T) = 0$. Solving for V_p yields,

$$V_p = \frac{qN_1 T^2}{2\varepsilon}. \tag{36}$$

Therefore,

$$E(0) = \frac{-1}{T}(V + V_p), \tag{37}$$

$$E(W) = \frac{-1}{T}(V - V_p), \tag{38}$$

and the final solution is,

$$E(x) = \frac{1}{\varepsilon} q N_1 x - \frac{1}{T}(V + V_p). \tag{39}$$

Equations (33) and (39) are the necessary results for calculating the breakdown voltage and the responsivity.

2.2.2 Avalanche Breakdown

The condition for avalanche breakdown can be determined from the continuity equations for holes and electrons. The analysis given here follows that of Sun *et al* [4], and is directly applicable to these structures. The analysis begins with the continuity equations,

$$\frac{dJ_n(x)}{dx} = \alpha_n J_n(x) + \alpha_p J_p(x), \tag{40}$$

$$\frac{dJ_p(x)}{dx} = - \frac{dJ_n(x)}{dx} . \tag{41}$$

Here the J_n and J_p are the electron and hole currents respectively, and α_n and α_p are the ionization coefficients for electrons and holes. For GaAs, these ionization coefficients are field dependent and are unequal [9]. As a result, the breakdown is highly dependent on these coefficients. Two equivalent expressions are used to solve for the breakdown condition. These expressions are obtained by considering the field where the current density tends to infinity from the continuity equations. They are as follows:

$$\int_0^T \alpha_p \exp \left[\int_x^T (\alpha_n - \alpha_p)\, dx' \right] dx = 1, \tag{42}$$

and

$$\int_0^T \alpha_p \exp\left[- \int_0^x (\alpha_n - \alpha_p)\, dx' \right] dx = 1. \qquad (43)$$

These relations have been used to calculate the breakdown voltages for GaAs EAP detectors with various doping levels and layer thicknesses. The results are shown in Figure 6. Values of the electric field were obtained from equations (33) and (39). The ionization coefficients used have the value and field dependence determined by Stillman *et al* [9].

2.2.3 Responsivity

The previously mentioned Franz-Keldysh effect can be observed as a variation in the absorption with the change in electric field, and hence, the reverse bias. Furthermore, the gain of the avalanche photodiode is also a function of the reverse bias. The net result is a change in the device responsivity with a change in the bias.

Responsivity is a figure of merit for the photodetector. It is defined as the current, I_{ph}, due to a flux of optical photons, ϕ_q, each with an energy equal to $\hbar\omega$.

$$R = \frac{I_{ph}}{\hbar\omega \iint \phi_q dA}. \qquad (44)$$

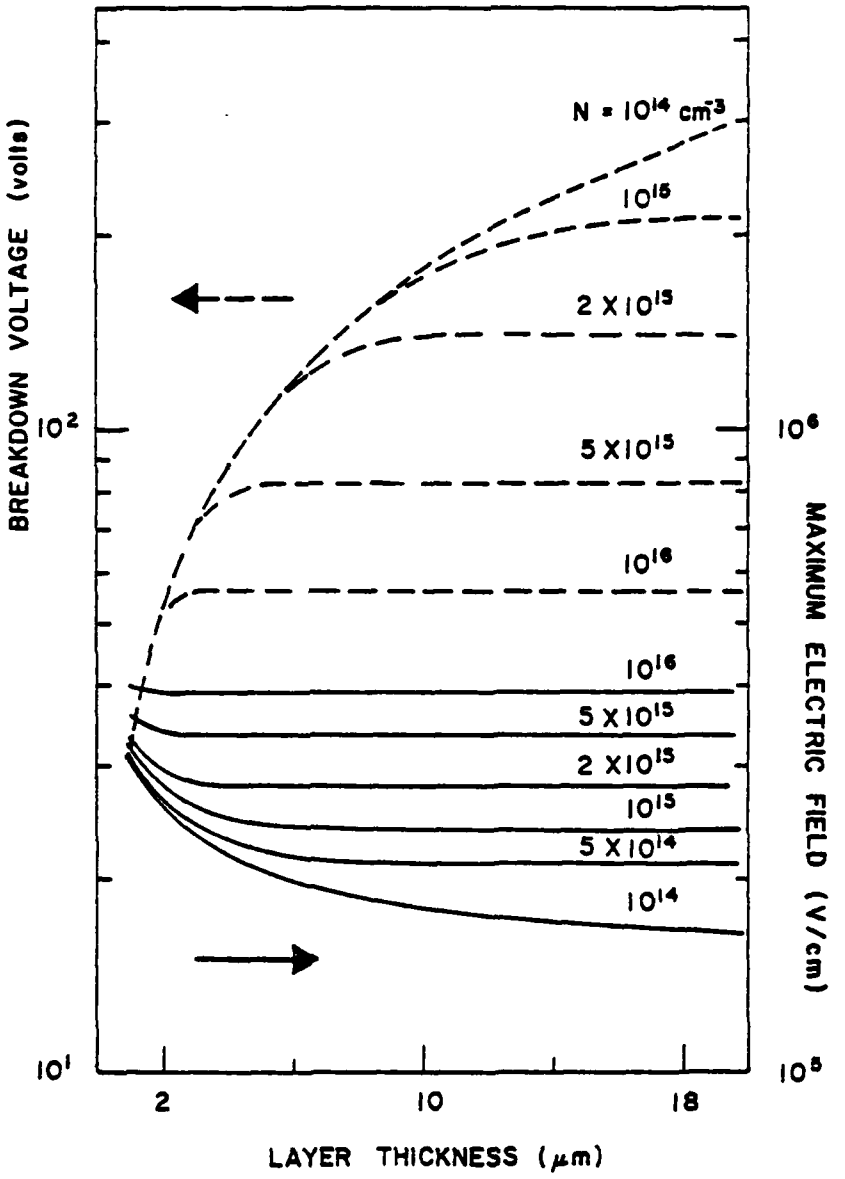

Figure 6 Breakdown voltage for the EAP detectors plotted as a function of the layer thickness and the doping level as a parameter.

To find the responsivity, the differential equations for the current density of the illuminated device must be obtained.

$$\frac{\partial J_n(x,z)}{\partial x} = \alpha_n(x) J_n(x,z) + \alpha_p(x)\ J_p(x,z) + qG(x,z), \quad (45)$$

$$\frac{\partial J_p(x,z)}{\partial x} = - \frac{\partial J_n(x,z)}{\partial x}\ , \quad (46)$$

$$J_n(x,z) + J_p(x,z) = J(z). \quad (47)$$

The ionization coefficients are now both spatially dependent since the field is spatially dependent. The generation of optically excited elctron-hole pairs is described by the function G(x,z). Evidently,

$$G(x,z) = - \frac{\partial \phi(x,z)}{\partial x}\ . \quad (48)$$

The absorption in the device causes an exponential decay in the flux density such that,

$$\phi(x,z) = \phi_i(x) e^{-\Gamma z}, \quad (49)$$

where the coefficient, Γ, is the absorption due to electroabsorption. Combining equations (47) and (48),

$$G(x,z) = \alpha(x) \phi_i(x) e^{-\Gamma z}, \quad (50)$$

where $\alpha(x)$ is the Franz-Keldysh electroabsorption coefficient.

Returning to equations (45, 46, 47) and using the integrating factor

$$P(\Lambda) = \exp\left[- \int_{o}^{\Lambda} \left[\alpha_n(\Lambda') - \alpha_p(\Lambda')\right] \, d\Lambda' \right], \tag{51}$$

one can obtain:

$$J_n(x,z) = \frac{1}{P(x)}\left[\int_{o}^{x} \left[J(z)\ \alpha_p(x') + qG(x',z)\right] P(x')dx' + J_n(0,z)\right]. \tag{52}$$

$J(z)$ is independent of x', and can be taken out of the first integral. Then from equation (47),

$$J_n(W,z) = J(z) - J_p(W,z). \tag{53}$$

Therefore,

$$J(z) = \frac{q\int_{o}^{W} G(x,z)P(x)dx + J_p(W,z)P(W) + J_n(0,z)}{P(W) - \int_{o}^{W} \alpha_p(x)P(x)dx}. \tag{54}$$

The responsivity can then be given as,

$$R = \frac{\int_{o}^{L} J(z)\ dz}{q\int_{-\infty}^{\infty} \hbar\omega\ \phi_i(x)\ dx} \tag{55}$$

Sun *et al* [4] have calculated equivalent electroabsorption coefficients for EAP waveguide detectors. Plots of responsivity using these results are shown in Figure 7.

2.3 FIELD EFFECT TRANSISTORS

The active device used for the response control is a Schottky barrier field effect transistor, (FET). The device structure is shown in figure 8. The gate is a self-aligned aluminum layer which is defined by a lift-off technique. The ohmic contacts to the source and drain are the typical gold-germanium (88% Au/ 12% Ge), nickel, gold metalizations which are alloyed at 456° C.

The channel resistance can be approximated for the unbiased FET as the resistance of the bulk semiconductor in the channel region,

$$R_{ch} = L/(aW\sigma_s), \tag{56}$$

where the conductivity of the region, σ_s, is given as

$$\sigma_s = qN\mu. \tag{57}$$

Here μ is the mobility of the majority carriers (electrons) in the region with a doping level of N carriers/cm^3. Therefore,

$$R_{ch} = L/(aWqN\mu). \tag{58}$$

The channel resistance affects the circuit operation in two ways. First, the FET acts as a variable resistor in series with the detector. For this reason, the resistance

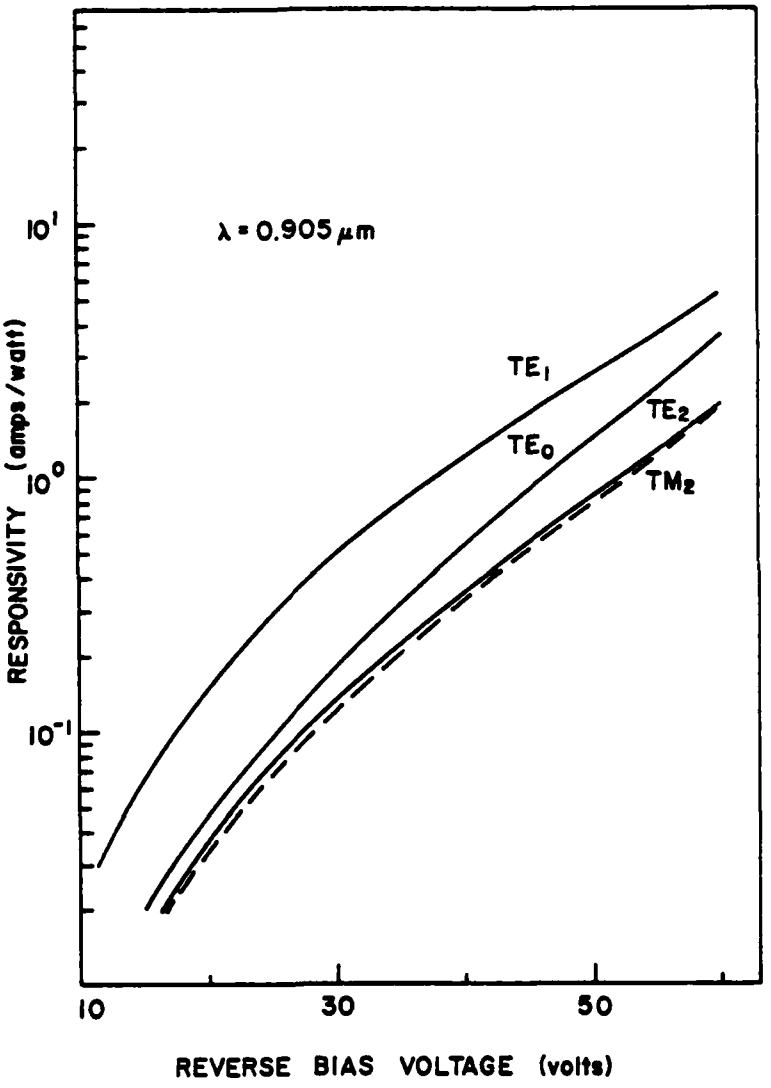

Figure 7 Calculated responsivity versus the detector reverse bias voltage.

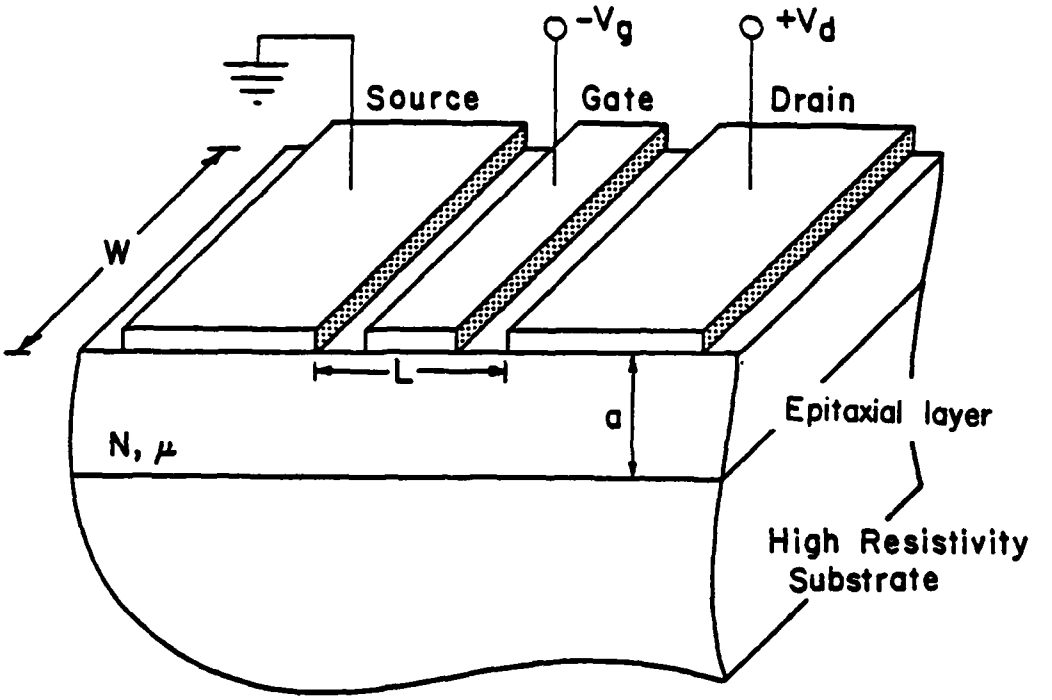

Figure 8 Illustration of Schottky barrier gate, GaAs field effect transistor.

must be small so that most of the detector bias will be across the detector and not the FET. Secondly, the power consumed by the circuit, and thus the heat produced will increase with the channel resistance. Both of these factors indicate that the channel resistance should be kept small.

A second consideration is the high frequency operation of the array. Later tests may require high speed sampling and multiplexing. Thus, a high speed FET is needed. The maximum frequency of oscillation, f_{max}, has been determined empirically for GaAs FETs with gate lengths, L, of 10 μm, or less [12] as follows:

$$f_{max} \simeq \frac{33}{L} \text{ GHz.} \tag{59}$$

Using the dimensions for this FET, L= 10 μm, W= 20 μm, and a doping density of 2×10^{15} cm^{-3} with a mobility of 4000 cm^2/ v-sec, one obtains,

$$R_{ch} = 78\ \Omega\ , \tag{60}$$

and,

$$f_{max} = 3.3 \text{ GHz} \tag{61}$$

These values are suitable results for the intended use of the system.

2.4 AUTOMATIC RESPONSE CONTROL

The automatic response control circuit consists of a feedback loop whereby the gate-to-source voltage of the FET is used as negative feedback to adjust the bias and hence, the responsivity, of an EAP detector. Figure 9 shows the circuit configuration. Coherent illumination of power, P, through a channel waveguide is incident on an EAP detector biased at voltage V_A. The FET is connected in the common gate configuration. The output of the circuit can be taken as V_A, V_G, or I_L. Resistor R_L is external to the chip as is the bias supply voltage, V_s.

2.4.1 Operation Below Saturation

In this analysis, we use the Shockley model for field effect transistors [13], and neglect the built-in potential of the gate-source junction. The equation for operation below transistor saturation is,

$$\frac{I_D}{I_P} = 3\,\frac{V_D}{V_P} - 2\left(\frac{V_D + V_G}{V_P}\right)^{3/2} + 2\left(\frac{V_G}{V_P}\right)^{3/2} . \qquad (62)$$

Here,

$$I_P = \frac{Wq^2\,\mu\,N_d^2\,a^3}{6\varepsilon L} , \qquad (63)$$

and

$$V_P = \frac{qN_d a^2}{2\varepsilon} . \qquad (64)$$

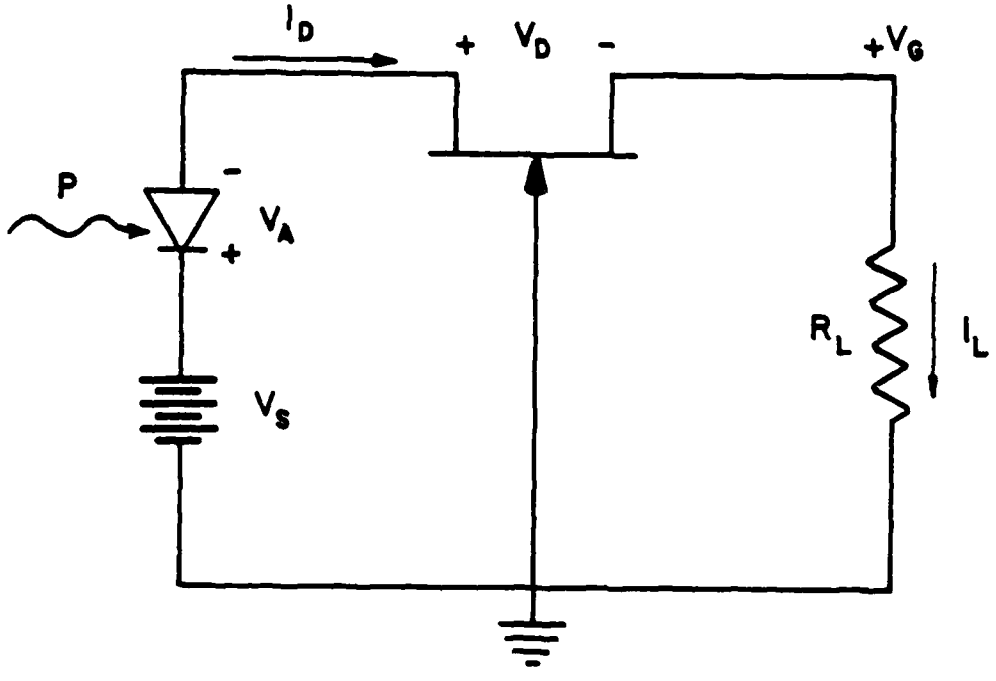

Figure 9 Automatic response control circuit.

The circuit itself adds the following constraints:

$$I_D = RP \,, \tag{65}$$

$$V_G = I_D R_L \,, \tag{66}$$

and

$$V_G = RPR_L \,. \tag{67}$$

Substituting these constraints into equation (62) gives,

$$\frac{RP}{I_P} - 3\,\frac{V_D}{V_P} + 2\left(\frac{V_D + RPR_L}{V_P}\right)^{3/2} - 2\left(\frac{RPR_L}{V_P}\right)^{3/2} = 0. \tag{68}$$

Equation (68) is analytically useful only if one can find some closed form for R. The responsivity data of Sun *et al* [4] demonstrates that near the excitation frequency of interest, R can be approximated by the function:

$$R = A \exp\,(BV_A) \,. \tag{69}$$

The constants A and B are determined graphically as in Figure 10. Now noting that

$$V_D = V_S - V_A - RPR_L \tag{70}$$

one obtains an equation relating the incident optical power to the bias across the EAP detector:

$$\left(\frac{PA \exp\,(BV_A)}{I_P}\right) - 3\left(\frac{V_S - V_A - PR_L A \exp\,(BV_A)}{V_P}\right)$$

$$+2\left(\frac{V_S - V_A}{V_P}\right)^{3/2} - 2\left(\frac{PR_L A \exp\,(BV_A)}{V_P}\right)^{3/2} = 0 \,. \tag{71}$$

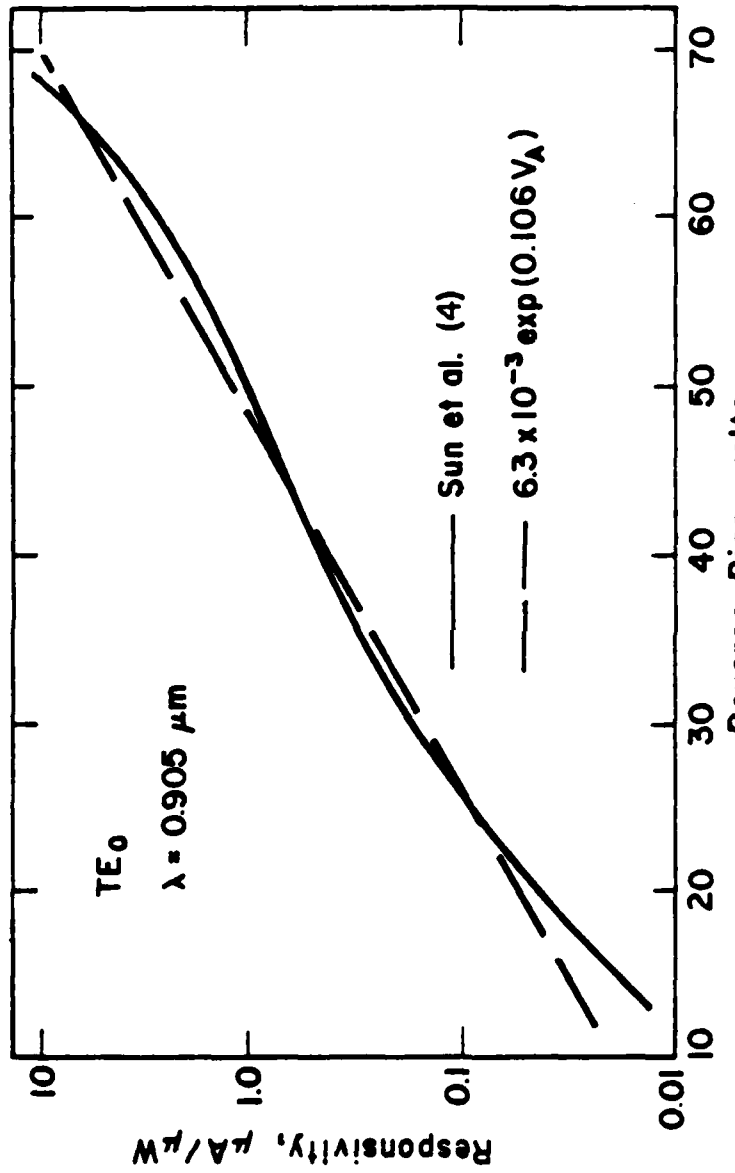

Figure 10 Functional approximation to responsivity data of Sun *et al* [4].

Some solutions of this equation for various values of V_S and R_L are plotted in Figure 11. Values for I_P and V_P were 6 milliamps and 1.2 volts respectively.

Equation (71) can also be used to find I_L as a function of the input power. Once V_A is found for a value of P, equations (65) and (69) determine the load current since

$$I_L = I_D \tag{72}$$

(if there is no leakage through the gate-source junction). Solutions of $I_L(P)$ are shown in Figure 12 for the parameters used in Figure 10.

2.4.2 Operation Beyond Saturation

The analysis of Section (2.4.1) does not take into account the saturation of the FET and subsequent saturation of the automatic response control. Using the Schockley model for a transistor in saturation [13], one obtains

$$\frac{I_D}{I_P} = 1 - 3\left(\frac{V_G}{V_P}\right) + 2\left(\frac{V_G}{V_P}\right)^{3/2}. \tag{73}$$

With the constraint of equation (66), this becomes

$$\frac{I_D}{I_P} = 1 - 3\left(\frac{R_L}{V_P}\right) I_D + 2\left(\frac{R_L}{V_P}\right)^{3/2} \left(I_D\right)^{3/2}. \tag{74}$$

This equation gives a unique solution for the saturation current, I_{DS}, in the automatic response circuit for a particular value of R_L/V_P. Expanding and collecting powers

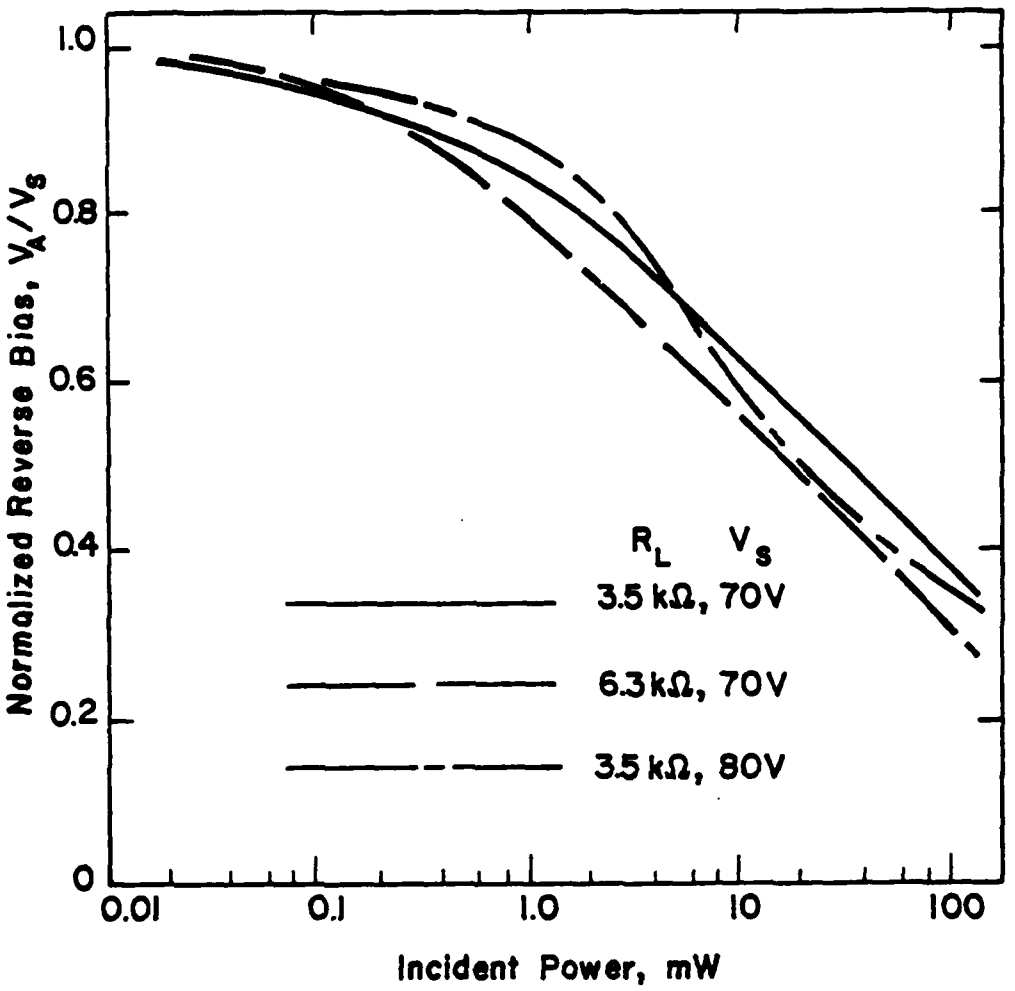

Figure 11 Calculated normalized reverse bias versus incident power for the automatic response circuit.

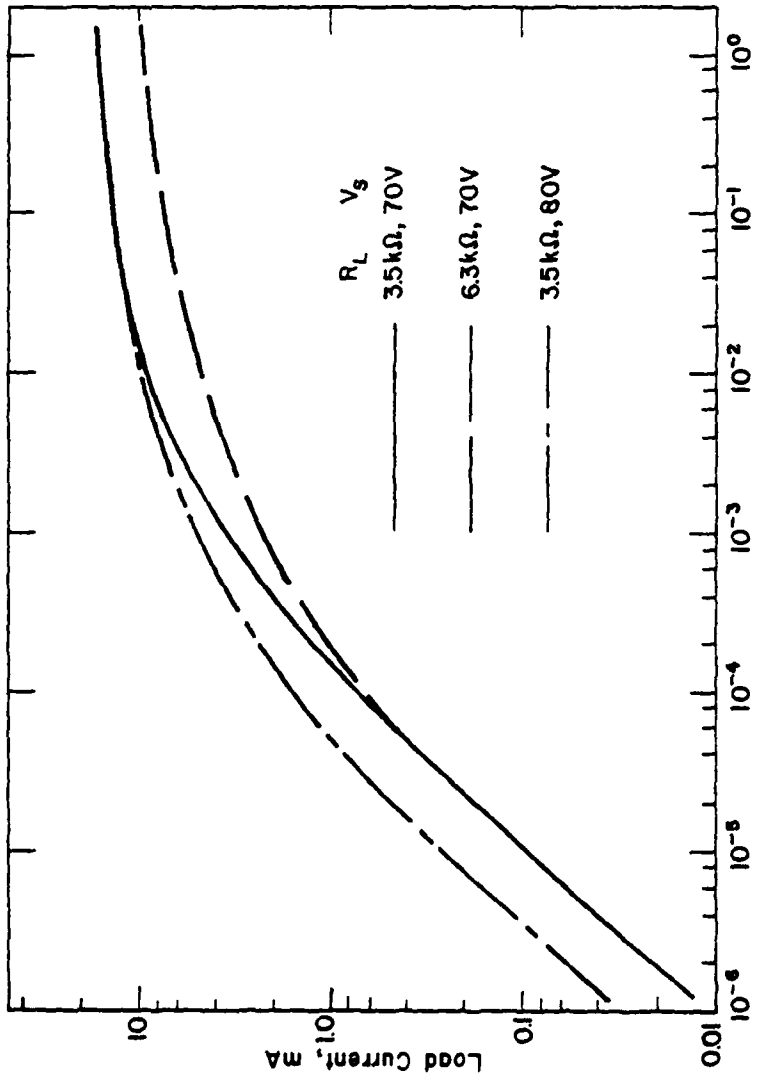

Figure 12 Calculated load current, I_L, versus incident power for the automatic response circuit.

of I_D gives the following result:

$$4\left(\frac{R_L}{V_P}\right)^3 I_{DS}^3 - \frac{1}{I_P^2} + \frac{6}{I_P}\frac{R_L}{V_P} + 9\left(\frac{R_L}{V_P}\right)^2 I_{DS}^2$$

$$+ \frac{2}{I_P} + 6\left(\frac{R_L}{V_P}\right) I_{DS} = 1 . \qquad (75)$$

If R_L is on the order of kilohms, V_P is a few volts, and I_P is a few milliamps, then the higher order terms in R_L/V_P will dominate and a simple cubic equation is left:

$$4\left(\frac{R_L I_{DS}}{V_P}\right)^3 - 9\left(\frac{R_L I_{DS}}{V_P}\right)^2 + 6\left(\frac{R_L I_{DS}}{V_P}\right) - 1 = 0. \qquad (76)$$

The meaningful solution to this equation is

$$I_{DS} = \frac{V_P}{4R_L} . \qquad (77)$$

There is also a root at $I_{DS} = V_P/R_L$, but this solution is inconsistent with equation (74). A graph of equation (77) is shown in Figure 13.

Equations (77) and (71) can be used to design optimum parameters for the automatic response control. Together, they indicate optimal operation for I_L taken as output when the load resistance is small and the pinch-off voltage is high enough to minimize the limitations of I_{DS}. If V_A is taken as the output of the circuit, the dynamic range is enhanced for large values of R_L. In this case, the effect of saturation is inconsequential.

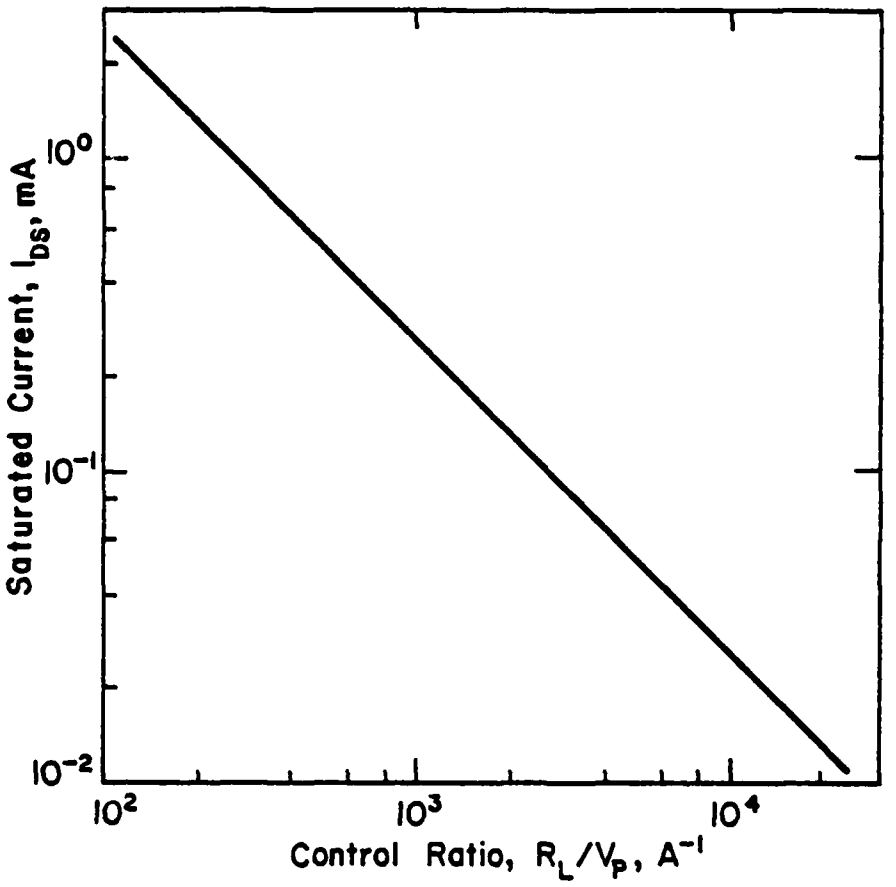

Figure 13 Saturated current I_{DS} versus control ratio R_L/V_p.

3. FABRICATION

The monolithic integration of the waveguide detector array requires a semi-insulating substrate with two epitaxial layers of different doping levels. This is accomplished by the method described in the following section. Processing of the subsequent material then required the development of photolithographic masks, followed by device fabrication, and evaluation. The methods for epitaxial growth and fabrication will now be considered.

3.1 EPITAXIAL GROWTH

The epitaxial layers were grown on chromium doped, semi-insulating substrates purchased from Laser Diode Laboratories. The orientation was chosen to be 2^{o} off the {100} plane to reduce the formation of hillocks. The measured resistivity for these substrates was typically 10^{7} ohm-cm.

3.1.1 Substrate Preparation

Before preparing the substrates, the wafers are cleaved into pieces approximately 2 cm on a side. These are then degreased by boiling successively in three solvents each for two minutes or more. The first solvent is trichloroethylene, followed by acetone and then methyl alcohol. The samples are then rinsed in deionized water with a resistivity of greater than 14 ohm-cm, and dried with bibulous paper in a laminar flow hood. Once the surface is degreased,

a chemical etch is prepared to remove some of the surface and thereby any contamination. The etch used is a mixture containing 5 parts sulfuric acid (H_2SO_4), to 1 part hydrogen peroxide (H_2O_2), to 1 part water (H_2O). The etchant is mixed and allowed to cool for 5 minutes. The sample is then etched for five minutes and rinsed in deionized water while being careful not to expose it to the air. After rinsing, the sample is again dried with bibulous paper under a laminar flow hood. The sample is then immediately placed in a pyrolytic SiO_2 reactor with the polished surface exposed. The reactor is sealed and two flows of N_2 at 4 liters/minute are introduced to flush the reactor for 4 minutes. The sample stage is heated to a temperature of 400°C. Flows of 100 ml/minute of 5% silane (SiH_4) in nitrogen and 40 ml/minute of oxygen are introduced and growth begins shortly. These conditions are maintained until the SiO_2 layer thickness is approximately 2500 Å which requires about 15 minutes. At this time, the oxygen and silane flows are shut off and the sample is allowed to cool to room temperature.

The SiO_2 is then defined so as to provide a mask for the growth of the first epitaxial layer. First, the sample is mounted on a glass microscope slide with black wax to provide support and ease in handling. The solvent degreasing is repeated to remove any trace of the black wax.

A furnace is heated to 130°C and the sample is baked for 20 minutes to remove any solvents, or moisture from the surface. After cooling, positive photoresist (type AZ1350B) is spun onto the sample at 3000 RPM for 30 seconds. The resist is then dried for 20 minutes at 70°C. The photoresist is exposed in an optical mask aligner for seven seconds. The mask used has lines and spaces that will open channels in the resist approximately 350 μm wide on 750 μm spacing. Developing is then done with a 50% solution of Azoplate developer and water in a spray bottle. The sample is rinsed for two minutes in deionized water and dried with forced nitrogen. Post-baking is done at 100°C for one hour to harden the resist. Now that the mask has been prepared, the SiO_2 is etched for 60 seconds in buffered hydrofluoric acid, and rinsed in deionized water. The photoresist and black wax are both removed by repeating the degreasing technique mentioned earlier. The sample is rinsed in deionized water and dried with bibulous paper. The 5 H_2SO_4 : 1 H_2O_2 : 1 H_2O etch is prepared and allowed to cool for 4 minutes. Etching is then done for 6 minutes which provides a 30 μm deep channel. The sample is then rinsed in deionized water, dried in bibulous paper and loaded into the epitaxial reactor.

3.1.2 First Epitaxial Growth

The epitaxial layers are grown in a vapor phase reactor which utilizes the $AsCl_3$:Ga:H_2 system. A schematic

drawing of the reactor and furnace is shown in Figure 14. The furnace is a single zone design which has been split to provide two zones. Each zone has an independent, solid state temperature controller. The reactor tube, bubbler, seed holder and melt boat are fabricated from Spectrosil quartz to insure a minimum of contaminants in the system. The system is air-tight and operates with positive pressure. Access to the system is obtained through a taper joint which is located on the downstream end of the furnace. Removal of the taper joint also removes the seed holder, and thus allows the seed to be loaded. A constant temperature water bath is provided to cool the $AsCl_3$ located in the bubbler.

The first epitaxial layer is required to be highly doped and approximately 30 μm thick. The layer serves two functions. First, as a low resistance contact to the diode detectors, and second, as a guiding layer for the waveguide in the second epitaxial layer. To achieve the desired doping level of 10^{18} cm^{-3}, 91 milligrams of tin (99.9999% purity) was added to the 10 gram gallium melt (99.9999% purity). This melt was placed in the furnace between the 14 and 17 inch points from the right hand side. This region provided a constant temperature across the melt to within 1°C. Before growth can occur, the melt must be saturated to form a GaAs skin on the surface of the melt. This is achieved by heating the melt to 840°C and

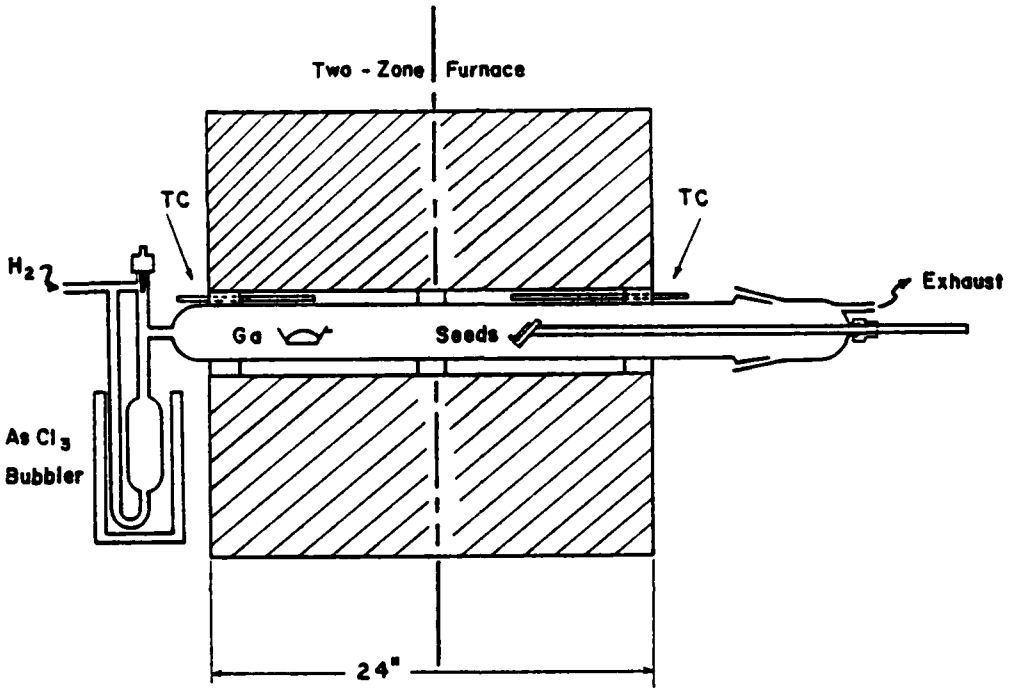

Figure 14 Schematic of epitaxial reactor and two-zone furnace.

the seed to 700°C for a period of 2 hours with a flow of hydrogen throughout the reactor at 150 ml/minute. During this time, the $AsCl_3$ is kept at a temperature of 6°C. Following this preheat, the seed zone is raised to 800°C, and the hydrogen flow is diverted through the $AsCl_3$ bubbler. After 3 hours the seed temperature is reduced to 740°C and the saturation continues for 3 more hours. At this time, the hydrogen flow is reduced to 30 ml/minute and the furnace is allowed to cool for 12 hours.

The seed, as prepared earlier, can now be loaded into the reactor and situated at the 5 inch mark from the right hand side. This point has a gradient of 20°C/inch. After loading, the furnace is flushed with purified hydrogen for 15 minutes with a flow rate of 210 ml/minute. The flow is then reduced to 150 ml/minute, the melt temperature set to 840°C, and the seed temperature set to 680°C. The $AsCl_3$ is maintained at 6°C throughout the growth cycle. After a three hour preheat, the seed temperature is raised to the growth temperature and allowed to stabilize for 15 minutes. The temperature is then raised to 770°C and the furnace shunted to provide a flat zone at the seed. This condition is allowed to stabilize for 15 minutes, then the hydrogen is diverted through the $AsCl_3$. During this time the substrate surface is etched and approximately 5 μm are removed during the 15 minute etch cycle. The furnace is then

returned to the unshunted condition and the temperature reset to maintain the seed at 740°C. As the furnace cools the etch rate decreases and growth begins. Growth is allowed to continue for 6 hours at a rate of 7 μm/hour. To terminate growth, the hydrogen is diverted around the $AsCl_3$, and the flow reduced to 30 ml/minute. The furnace is turned off and allowed to cool for 12 hours. The seed is removed and measured for layer thickness and doping level. A cross-section of the growth is shown in the photograph of Figure 15.

3.1.3 Second Epitaxial Growth Preparation

Considerable overgrowth occurs from the first epitaxy which must be removed before the second growth. The procedure involves lapping to give a flat surface that is oriented parallel to the original surface. The lapping begins by selecting a flat polishing plate. Next the sample is mounted in a jig that is designed to maintain the surface parallel to the plate. The back of the sample is lapped first to provide a flat mounting surface. This procedure does not in general result in the epitaxial surface being mounted parallel to the plate. However, by using a worn plate, this problem can be avoided. The used or worn plate is concave with the center lower than the outer rim. Once the sample mounting has been determined to be incorrect, it can be aligned on the worn plate so that

(a)

(b)

Figure 15 Photographs of sample cross-section showing growth of n^+ layer.
(a) unstained section
(b) section after staining

the plate surface is nearly parallel to the desired surface on the sample. Thus, by trial and error, the surface can be made parallel to the desired surface. This requires good judgement, but is not hard to learn. After the sample is oriented, a flat plate can be used to finish the lapping and obtain a flat surface. The sample is then removed from the jig and degreased in the organic solvents. An etch was then done in hydroflouric acid to remove any remaining SiO_2, followed by a rinse in deionized water. The sample was then prepared for growth by etching in 5 H_2SO_4: 1 H_2O_2: 1 H_2O for 25 seconds after cooling for 10 minutes. This etch removed about 5 μm of the GaAs and provided a much smoother and cleaner surface for growth.

3.1.4 Second Epitaxial Growth

The sample was then loaded into the same reactor as before. The melt this time contained 10 grams of high purity gallium with two 0.010 inch diameter tin spheres. Saturation of the melt was performed as in section (3.1.2). This melt produced a doping level of between 1 and 3×10^{15} cm^{-3}. The growth is performed as in section (3.1.2) with the exception that the growth temperature was raised to 745°C and the growth time reduced to 30 minutes. This resulted in a layer approximately 5 μm thick. Figure 16 (a,b,c) is a schematic representation of these steps.

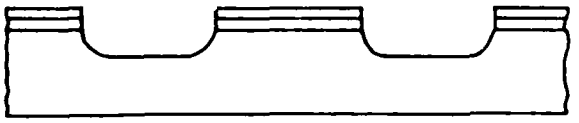

(a) Substrate prepared for first epitaxial growth.

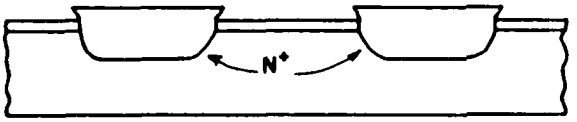

(b) Sample after first epitaxial growth.

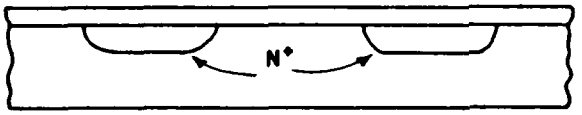

(c) Sample after second epitaxial growth

Figure 16 Process schematic for epitaxial growth

3.2 DEVICE PROCESSING

Once the epitaxial growth is completed, device processing can begin. The waveguide detector array is implemented in a 30 channel device as is shown in Figure 17. Some of the channels have been deleted to save space. The cross section shows the two epitaxial layers and the location of the active components relative to them. Each process step will be explained in some detail followed by a schematic diagram of the result. Figure 18 shows the substrate prior to the second epitaxial growth. The dark areas are the conducting epitaxy which are arranged in strips so that the structure is periodic. The arrays are lined up in rows each with one conducting strip to provide contact to the diode detectors.

3.2.1 Isolation Etch

The first fabrication step provides a channel in the second epitaxial layer so that the FET active region is isolated from the low resistance contact to the detector. An SiO_2 layer is grown as in section (3.1.1) with a thickness of 11(Å. The sample is then mounted on a glass microscope slide with black wax. The solvent degreasing is performed to remove residual black wax and other organic contaminants. A furnace is heated to 105°C and the sample baked for 5 minutes. After cooling for 5 minutes, positive photoresist is applied (type AZ 1350B) and spun for

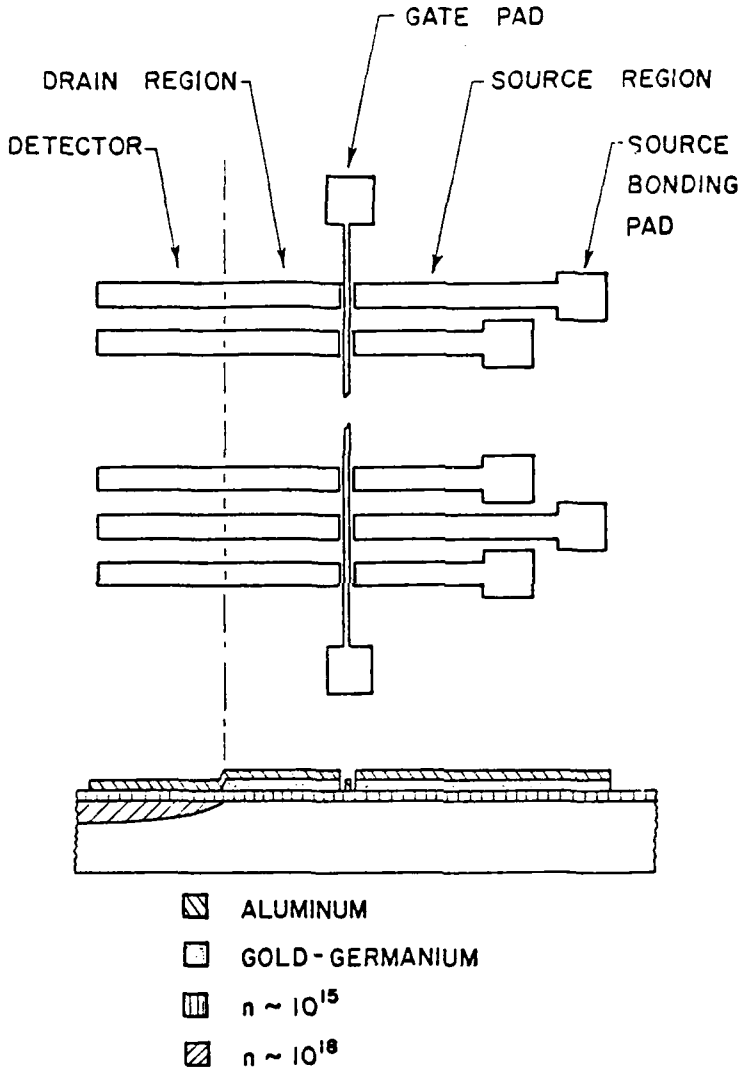

Figure 17 Illustration of 30 channel array implemented on GaAs.

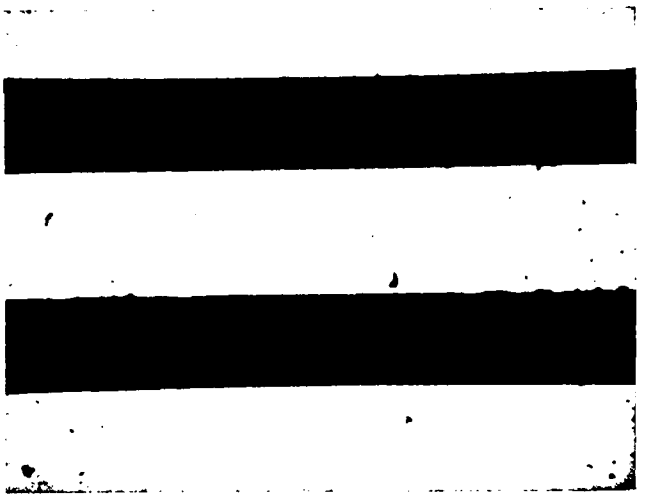

Figure 18 Photograph of the sample surface after lapping the overgrowth from the first epitaxial growth. The dark regions are n^+ GaAs and the light areas are SiO_2 on the GaAs substrate.

30 seconds at 3000 RPM. The photoresist is then dried at 100°C for 30 minutes and cooled for 5 minutes. An optical mask aligner is used to expose the photoresist after which it is spray developed for 45 seconds in a 50% solution of Azoplate developer in deionized water. Developing is followed by a 2 minute rinse in deionized water and drying in forced nitrogen. The sample is then baked at 105°C for one hour to harden the resist.

Three beakers are set up for the SiO_2 etch with two containing rinse water and one containing buffered hydrofluoric acid. The sample is dipped in the first rinse beaker briefly, and then in the HF for 5 seconds. A second rinse is done for 10 seconds and the sample is then inspected under the microscope to see if the SiO_2 has been removed. This is continued using shorter etch times until the SiO_2 is completely removed. Typical etch times are 7 seconds. The sample is then rinsed well in deionized water and then in acetone to remove the photoresist. The 5:1:1 etch is prepared as in section (3.1.1) and allowed to cool for 10 minutes. Once the etch is at room temperature, the etch rate is nearly constant at 12 μm/minute. The GaAs is then etched for 35 seconds to remove 7 μm, and rinsed in deionized water for 1 minute. The sample is then dried with forced nitrogen and is then ready for the next step. Figure 19a shows the sample with the isolation etch completed.

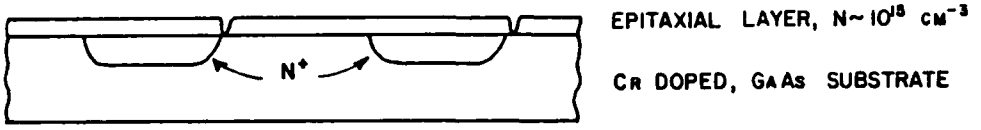

(a) Sample with isolation etch completed.

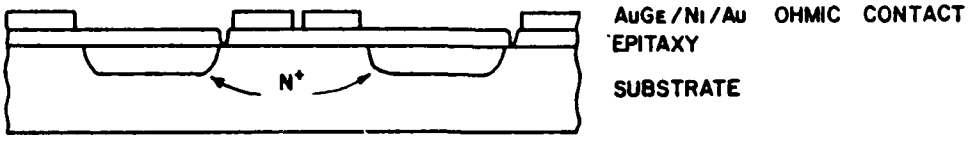

(b) Ohmic contacts after lift-off.

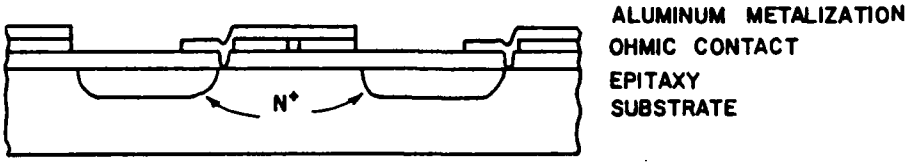

(c) Aluminum metalization on top of ohmic contacts.

Figure 19 Schematic representation of the isolation etch, ohmic contact lift-off, and aluminum metalization.

3.2.2 Ohmic Contacts

Standard ohmic contacts are used for the FET which are defined with a lift-off technique. The sample is pre-baked at 85°C for 15 minutes and then cooled for 5 minutes. Photoresist type AZ1350 J is spun onto the sample at 6600 RPM for 60 seconds and baked at 70°C for 30 minutes. The spin and bake is repeated two more times to provide a very thick coating (approximately 3 μm) necessary for covering the isolation channel. After cooling for 5 minutes the sample is exposed for 15 seconds and spray developed with the 50% Azoplate solution for 45 seconds. Deionized water is then used to rinse the sample for 2 minutes after which the sample is dried with forced nitrogen. Next, the sample is loaded into a vacuum evaporation system and a three layer metalization is deposited. The first layer is 1400 Å of the eutectic alloy gold-germanium (88% Au/ 12% Ge). The second layer is 500 Å of nickel. This is followed by the third layer of gold, 1500 Å thick. Next, the sample is removed from the vacuum and immersed in acetone to dissolve the photoresist. A squirt bottle of acetone is used to remove the metalization, thereby finishing the lift-off. The samples are then boiled in acetone to remove any remaining photoresist, and dried with forced nitrogen. Alloying of the contacts is done in a constant temperature furnace. The sample is loaded at the cool end of the furnace

and a flow of 200 ml/minute hydrogen is used to flush the furnace tube. After a 3 minute flush the samples are moved to the hot zone which is held at 456°C for 45 seconds and then returned to cool in the original position. The samples are removed from the furnace and mounted with black wax for the next process step. The result is shown in Figure 19b. Photographs of the contacts are shown in Figure 20 before and after alloying.

3.2.3 Mesa Formation

A second evaporation is required in which aluminum is deposited to a thickness of 4000 Å. This is followed by the application of the three coats of photoresist AZ 1350 J as in Section (3.2.2). Exposure time was 25 seconds this time, and the development was increased to 2 minutes to remove the resist completely from the isolation channel. The sample is rinsed as before in deionized water and dried with forced nitrogen. Postbaking is done at 110°C for 90 minutes. Etching of the aluminum requires a cyanide solution which is obtained from Metex and is known as Aurostrip. The etch solution is maintained at 38°C during the etch and is agitated by a stream of nitrogen introduced through a fritted disk. This method is commonly referred to as a bubble etch. The sample is mounted over the solution, so that when the nitrogen flow is started, the bubbles burst on the sample. In this way, the etchant is transferred to the sample with significant agitation allowing the etching of very fine

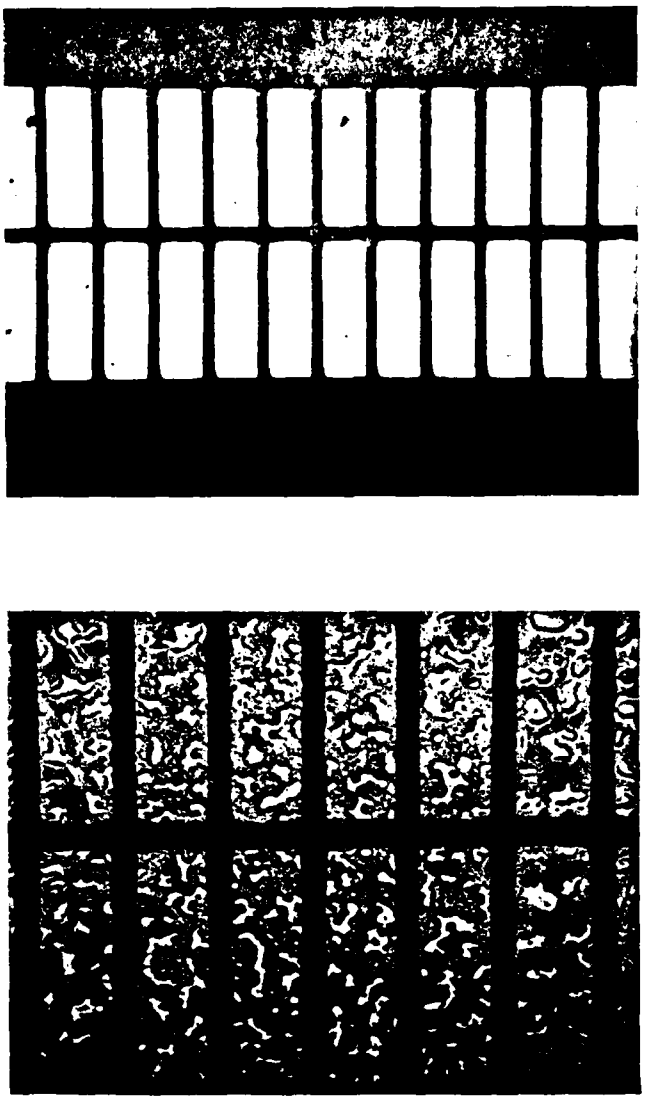

(a)

(b)

Figure 20 Photograph of ohmic contacts
(a) before alloying
(b) after alloying

lines. Features in the photoresist as small as 2 μm have been etched in this way. Once the sample has been etched for 2 minutes, it is removed, rinsed in deionized water, and checked with a microscope to observe the etch progress. Etching is then continued until the desired aluminum is removed. The sample is then degreased to remove the resist and prepare it for the channel etch. This etch forms the mesa for the waveguides and the FETs. The aluminum is used as the mask and is not attacked during the etch. The etchant is mixed using 1 part H_2SO_4 to 8 parts H_2O_2, to 1 part deionized water. After cooling for 10 minutes, the sample is immersed for 21 seconds during which time 7 μm are removed. The photograph in Figure 21 shows the aluminum mask after the channel etch. In the region where the aluminum crosses the isolation channel, (formed in Section (3.2.1)), the aluminum widens showing that the resist mask was not fully exposed in the channel. As this did not affect the device operation, no changes were made to correct this. (See Figure 19c for Schematic.) Photographs have been included in Figure 21 to show the aluminum mask and the mesa structure.

3.2.4 Gate Lift-off

The FET gate is formed by a self aligned lift-off technique. Three coats of resist AZ 1350 J are applied as previously, exposed for 2 minutes, and developed for 3 minutes. This is again rinsed with deionized water and

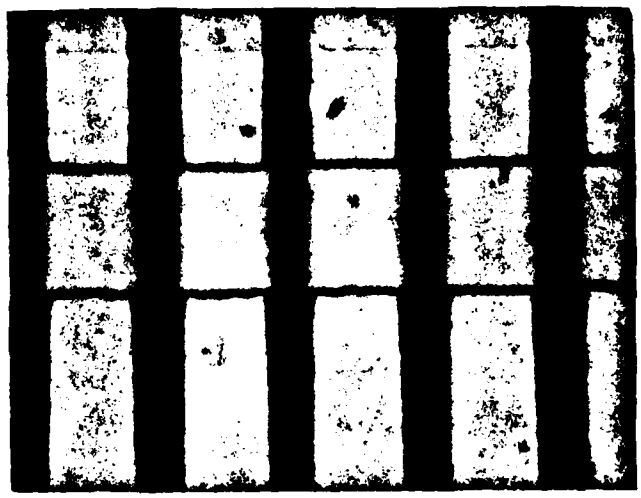

(a)

(b)

Figure 21 Photographs of etched mesa near isolation channel.

(a) optical micrograph showing aluminum mask

(b) SEM photograph showing waveguide mesa and isolation channel

dried with forced nitrogen. Postbaking is not done to make the lift-off easier. A bubble etch is again used with Aurostrip to remove the aluminum from the FET channel region. The aluminum is undercut so that the resist overhangs the aluminum. Aluminum is then deposited by evaporation in vacuum. The sample is then soaked in acetone to remove the resist and the undesired aluminum. A squirt bottle of acetone was also used to help in the removal of the aluminum. This procedure was not altogether successful. The aluminum tended to adhere to the channel region, but did not remain between the FET and the gate contact pad. Thus, the gates were well defined but there was no means to contact them. This result is shown schematically in Figure 22a,b. Several photographs were taken of the different results obtained from the gate lift-off. Figure 23a shows the aluminum gate on a sample with no ohmic contacts or mesa. As can be seen the result is quite good. The gate is 5 μm wide and with the undercut shown, would allow a source-drain spacing of 10 μm. This was the desired result. In the second photograph, (Figure 23b) the gate is shown aligned on the ohmic contacts, but without the mesas. Again, the result is as desired. Notice that the gates are all connected to a single common gate bonding pad. Figure 24 shows another result with the mesa, but without the ohmic contacts. In Figure 24a, the gate did not adhere, however, the etch was good and the aluminum is well defined in the channel

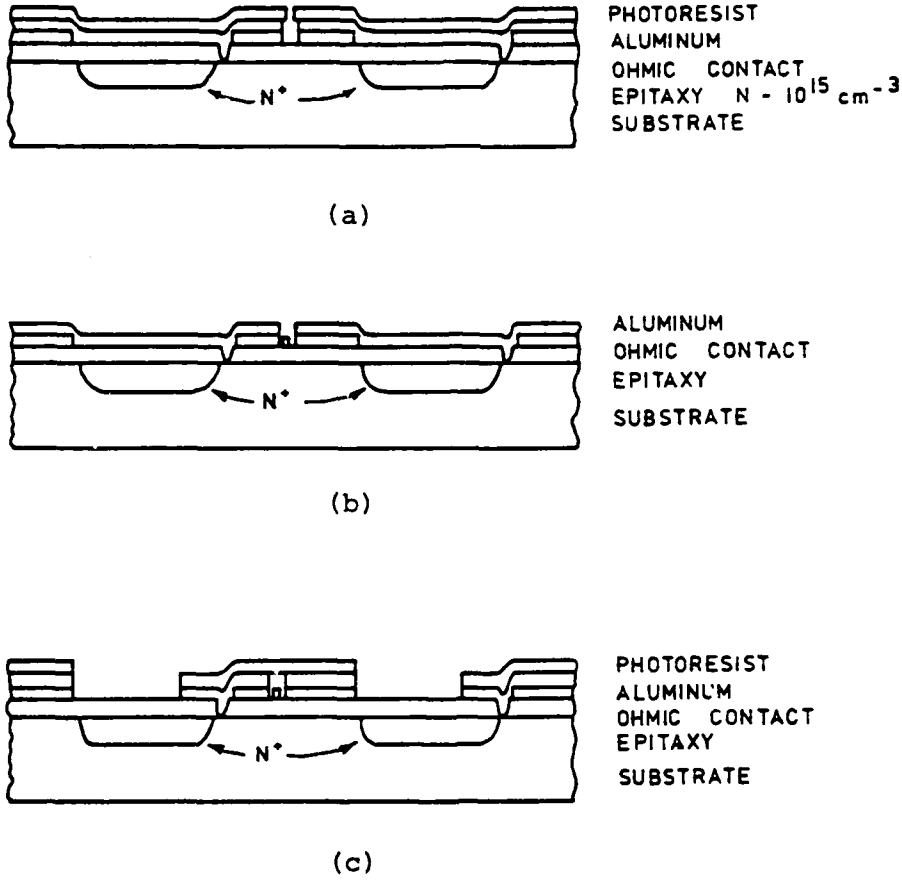

Figure 22 Schematic representation of gate lift-off

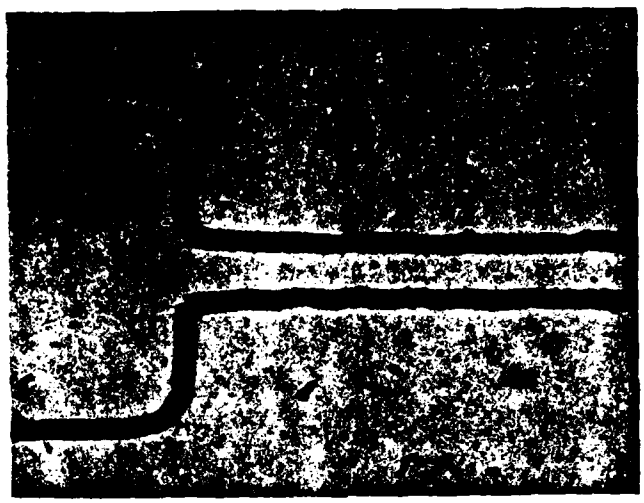

(a)

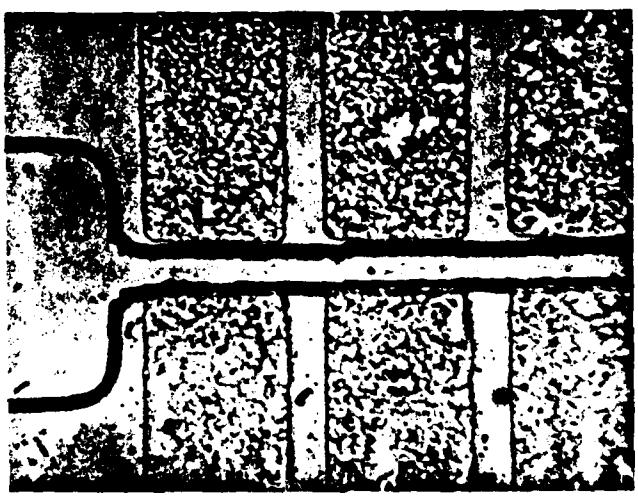

(b)

Figure 23 Photographs of aluminum self-aligned gate.

(a) on sample surface with no ohmic contacts or mesa structure

(b) on surface with ohmic contacts, but no mesa structure

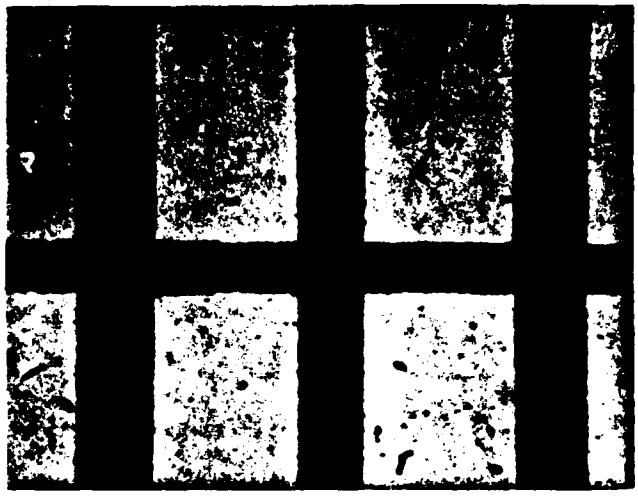

(a)

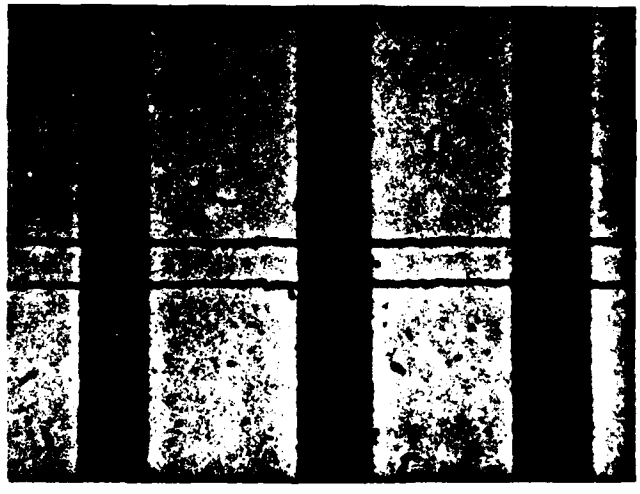

(b)

Figure 24 Photographs of aluminum mask after the mesa etch.

(a) gate did not adhere to FET channel during lift-off

(b) gate adhered to the channel, but not elsewhere

region. Figure 24b shows a similar result in which the gate did adhere to the channel but was not connected between the FETs or to the gate bonding pad. Here, the undercut was not sufficient to give the 5 μm gate. The final pair of photographs (Figure 25) shows the aluminum mask on the mesa with the ohmic contacts. The photograph in Figure 25a shows the sample before the gate etch and lift-off. In the Figure 25b photograph, the channel region has been etched and the gate evaporated and lifted. The result looks quite good except that the gates are not connected to each other or to the common pad.

3.2.5 Photodetector Delineation

The final step requires a repeat of the 3 coats of resist AZ 1350 J exposed for 30 minutes and developed for 2 minutes. The resist is then dried for 90 minutes at 110^{o}C. This mask covers the EAP detector and allows the removal of the remaining aluminum from the waveguide. The bubble etch is repeated with the Aurostrip for approximately 10 minutes. The sample is checked with the microscope to see that all of the required aluminum is removed. The photoresist is then removed in acetone. This provides the final device structure. Figure 22c shows the resulting profile.

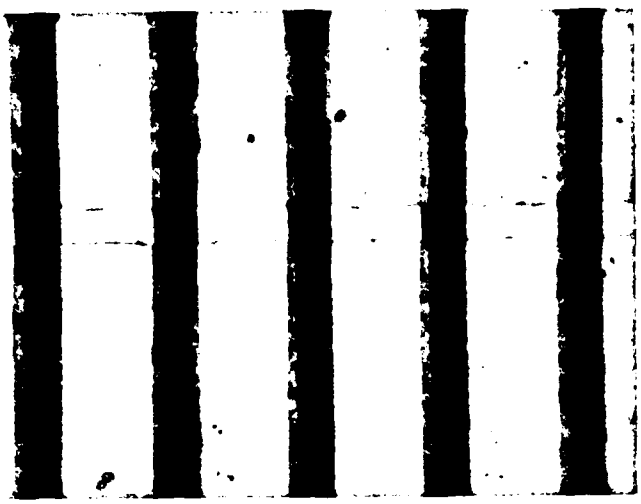

(a)

(b)

Figure 25 Photographs of the channel region with the ohmic contacts and the mesa structure.

(a) before the channel is etched for the gate lift-off

(b) after the gate lift-off

4. EVALUATION

The device processing was terminated at section (3.2.4), after the gate lift-off. To obtain data on the detectors, a device array was used that had been fabricated without the FETs. The data presented here are from this array, and are typical of other arrays processed similarly.

For the evaluation, the samples were cleaved and mounted on headers. Although different methods were tried, uniform cleaves were difficult to obtain. This becomes a problem when trying to couple the laser to the waveguide. It is difficult if not impossible to compensate for the quality of the cleave. Two lasers were used to obtain the entire dynamic range of the evaluation. For larger power levels, a 5 watt pulsed laser was used operating at 0.905 μm. Below 1 μwatt, a CW laser was used operating at 0.89 μm, and 5 milliwatt output. Although every attempt was made to obtain these data accurately, noise limited the dynamic range for both lasers. For pulsed operation, noise originated in the circuits used to drive the laser and was not due to the photodiode array. CW measurements were limited to variations in the dark current due to microplasma breakdowns. Although such breakdowns are fairly common, their effect can be minimized by careful material preparation and selection.

4.1 EQUIPMENT

A specially designed probing apparatus allowed easy mounting of the device headers. The device was viewed with a microscope allowing careful alignment of two tungsten probes. Movement of the probing apparatus was provided by an X-Y-Z-θ translator to place the device in the laser beam focal plane. The laser and associated optics were each mounted on X-Z translators fixed to a common X-Y translator. This common translator provided convenient scanning of the detector array. The optics chosen for focusing the laser beam were two infrared lenses and one microscope objective.

The electrical connections are shown in Figures 26 and 27. For pulsed operation, an oscilloscope was necessary to measure the response across the 50 ohm load. Two configurations are shown utilizing the scope single input and differential inputs. A slight reduction in noise was noticed for the differential mode, but some versatility and accuracy was also lost. All connections were made with standard 50 ohm coaxial cable and fittings to minimize noise pickup. For the CW measurements, the scope was not used, and the photocurrent was measured directly with a digital current meter. Coaxial cable was also used for these measurements to reduce noise.

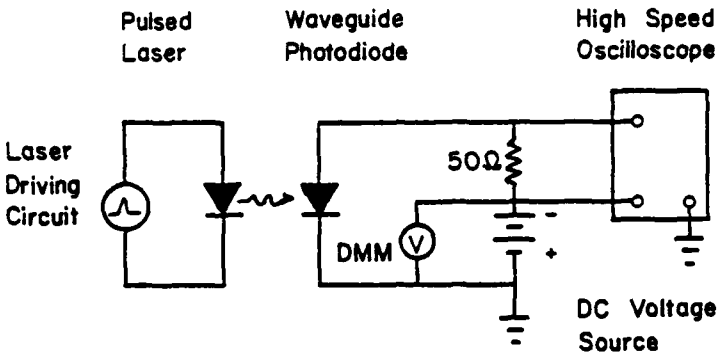

(a) Differential input to the scope

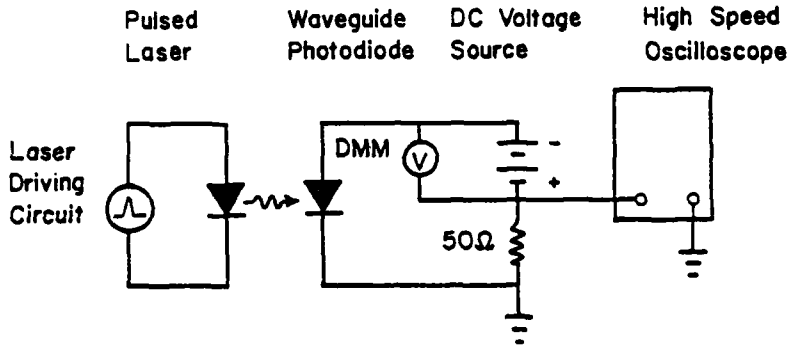

(b) Single input to the scope

Figure 26 Electrical connections for pulsed measurements.

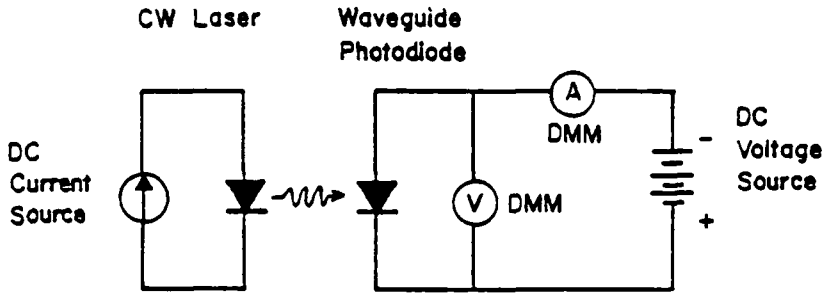

Figure 27 Electrical connections for CW measurements

4.2 PROCEDURE

The pulsed laser was connected and set to operate at a 200 nsec pulse width and 2kHz PRF. This mode of operation results in a small duty cycle to maximize laser stability. A power meter was mounted in place of the detector during alignment. The optics were then arranged for maximum response. An aperture was placed at the beam focal point. The aperture size was 5 by 20 μm: the same as the waveguide input face. By measuring the power transmitted through this aperture, the amount of light incident on the waveguide could be calibrated. After calibration, the power meter and aperture were replaced by the waveguide photodetector array. The alignment was repeated for maximum response. Bias supplied to the detector was also varied for a maximum signal. Response at reduced power levels was then obtained by reducing the laser current and by introducing neutral density filters into the beam.

4.3 RESULTS

Data have been collected using several detectors and a variety of techniques to insure the consistency of the results. Both pulsed and CW lasers were necessary to achieve the high and low power levels, respectively. The accuracy of these data is limited to the values shown in Figure 28. This is a best case analysis and does not include errors due to locating a maximum in response or variations arising from the quality of the cleave.

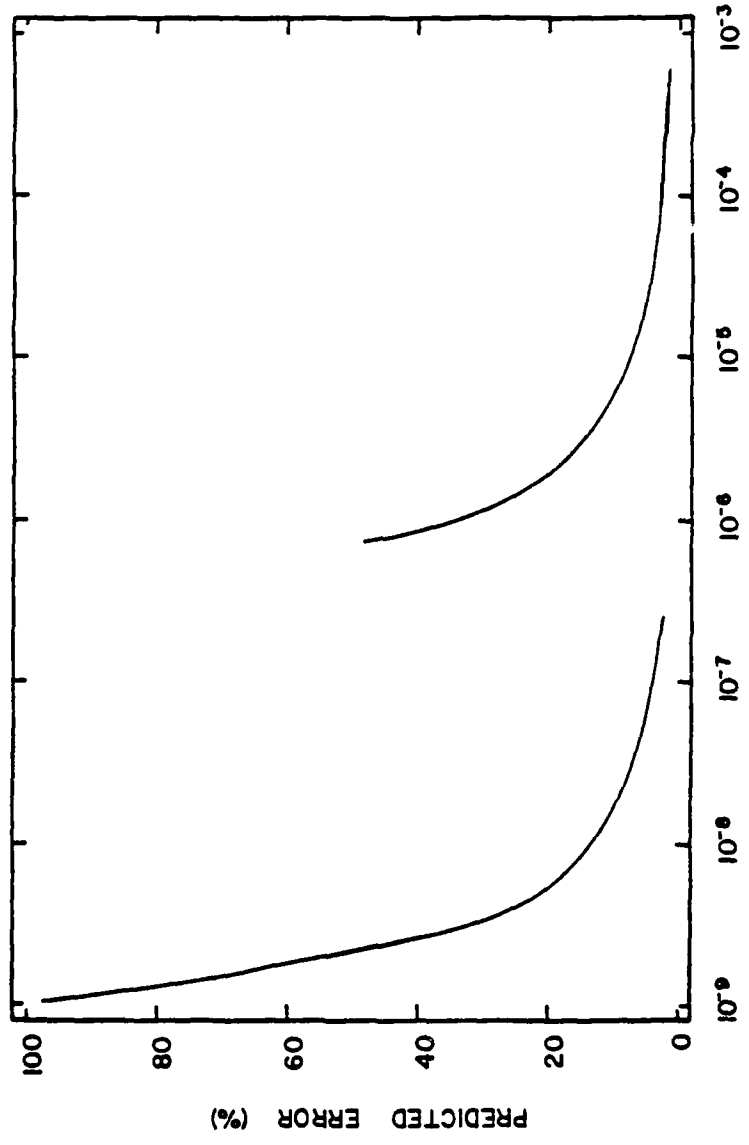

Figure 28 Predicted minimum error.

4.3.1 Pulsed Laser Data

A row of 50 detectors was chosen for study. The first 30 of these were good quality, but the remaining 20 decreased in quality as the sample edge was approached. Each of the 30 was illuminated with the 0.905 μm laser at maximum power and at reduced power levels until the response was undetectable. All detectors were biased at the same dark current. The laser was swept along the array and maximized for each detector so as to reproduce the same illumination for each detector. These results are listed in Table 1. Next, a suitable detector was chosen for dynamic range data. For this detector the power was varied in smaller increments to provide a larger number of data points.

4.3.2 CW Laser Data

CW measurements were done only for the purpose of extending the dynamic range data. Power levels were set by using neutral density filters. The power was reduced until the response was no longer detectable. These data were obtained with a different detector than that obtained with the pulsed laser.

4.4 ANALYSIS

The role of the waveguide photodiode array is crucial in providing accurate Fourier transform data in a spectrum analyzer. Any analysis of the array must take into account the dynamic range requirements as well as the uniformity of

Table 1
Response of Scanned 30 Element Array

element no.	Power level (dB)				bias voltage
	0	-4.3	-8.9	-13.2	
1	2.28	1.2	0.60	0.40	76
2	2.40	1.3	0.80	0.50	77
3	2.40	1.4	0.60	0.40	79
4	2.40	1.3	0.60	0.40	82
5	2.40	1.2	0.60	0.50	82
6	2.60	1.2	0.60	0.40	88
7	2.60	1.3	0.60	0.30	85
8	3.00	1.2	0.60	0.40	86
9	3.00	1.6	1.1	0.70	80
10	3.00	1.4	0.60	0.40	93
11	2.70	1.1	0.50	0.40	89
12	3.00	1.4	0.30	0.50	93
13	2.60	1.3	0.60	0.20	87
14	3.20	1.8	0.60	0.20	90
15	2.90	1.5	0.70	0.40	93
16	3.20	1.6	0.60	0.30	94
17	2.80	1.4	0.50	0.30	93
18	2.80	1.0	0.30	----	86
19	2.00	0.6	0.10	----	90
20	3.80	1.8	1.00	0.30	94
21	3.20	1.6	0.50	0.40	95
22	4.50	2.2	1.2	0.60	96
23	4.60	2.2	0.90	0.50	102
24	3.60	2.4	1.4	0.60	104
25	3.20	1.4	0.80	0.60	102
26	4.00	1.6	1.2	0.80	103
27	4.20	2.8	1.2	0.40	97
28	2.40	1.6	0.20	0.40	100
29	2.30	1.2	0.60	0.30	95
30	2.00	1.2	0.40	0.20	110

the response. Crosstalk must be minimized to allow the full use of the dynamic range.

4.4.1 Dynamic Range

Photoresponse has been measured for a total power range of 57 dB. The data taken with the pulsed laser account for 29 dB and the remaining 28 dB were taken with the CW laser. A curve was fitted to these data by linear regression. Deviations from the curve were then computed both in percent and in dB. Table 2 lists these data along with the computed deviations from the curve. The data are plotted along with the curve in Figure 29. Figures 30 and 31 are plots of the deviations. The equation for the best fit curve is as follows:

$$I_{ph} = k\ (P)^{0.5182}$$

where I_{ph} is the photoresponse

P is the incident power

$k = 0.1012$; I_{ph} (amps), P (watts)

or 78.67 ; I_{ph} (μamps), P (μwatts)

Deviations must be considered with respect to the error estimate given in Figure 28.

4.4.2 Channel-to-channel Tracking

The analysis of 30 adjacent photodiodes provided information on response uniformity. Each detector was illuminated in the same way and at the same power levels. Therefore, any variation is due to the variation in the photodiode. The response data (as given in Table 1) are

Table 2

Dynamic range data

P_i (uwatt)	I_p (uamp)	I_p" (uamp)	$\frac{I_p - I_p"}{I_p}$ (%)	10 log (I_p/I_p")
540	2600	2051	26.8	1.03 dB
188	1150	1187	- 3.1	-0.14
75	640	737	-13.2	-0.61
70	620	711	-12.8	-0.59
64	600	679	-11.6	-0.54
53	580	616	- 5.8	-0.26
44	520	559	- 7.0	-0.31
35	500	497	0.6	0.03
26	460	426	8.0	0.33
22	400	390	2.6	0.11
14	320	309	3.6	0.15
9.0	260	246	5.7	0.24
6.0	200	199	0.5	0.02
3.5	160	151	6.0	0.25
2.2	120	118	1.7	0.07
0.7	40	65.4	-39	-2.1
0.23	39	36.7	6.3	0.26
0.068	21	19.5	7.7	0.32
0.025	12	11.6	3.4	0.15
0.0075	6	6.23	-3.7	-0.16
0.0037	4	4.32	-8.0	-0.33
0.0011	1	2.31	-53	-3.6

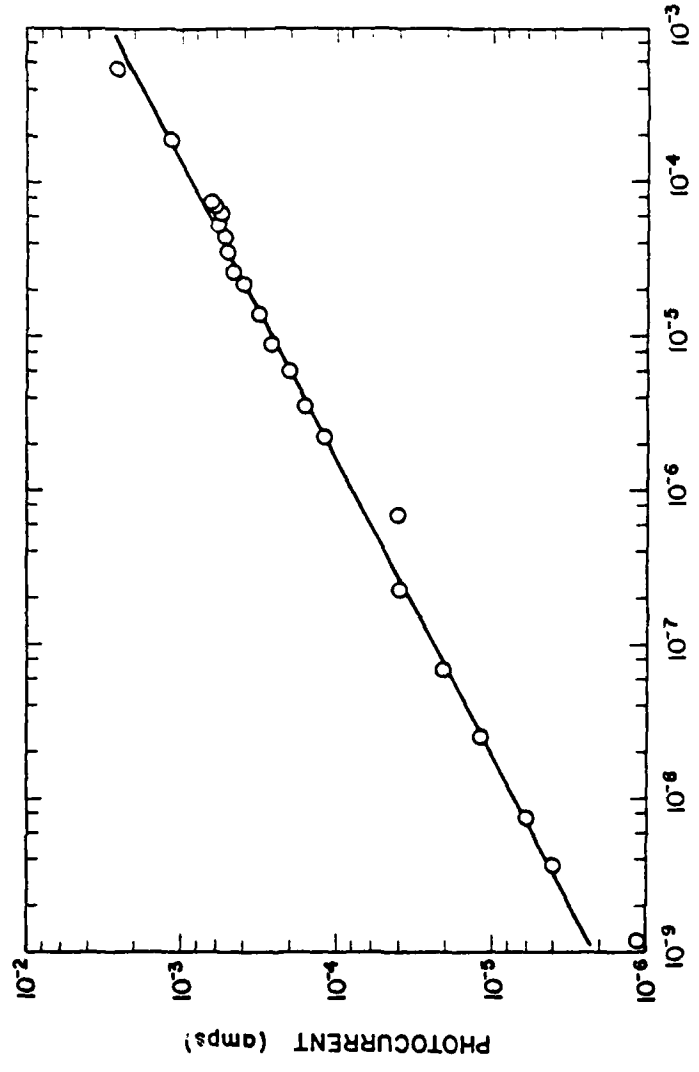

Figure 29 Response characteristic for an EAP detector.

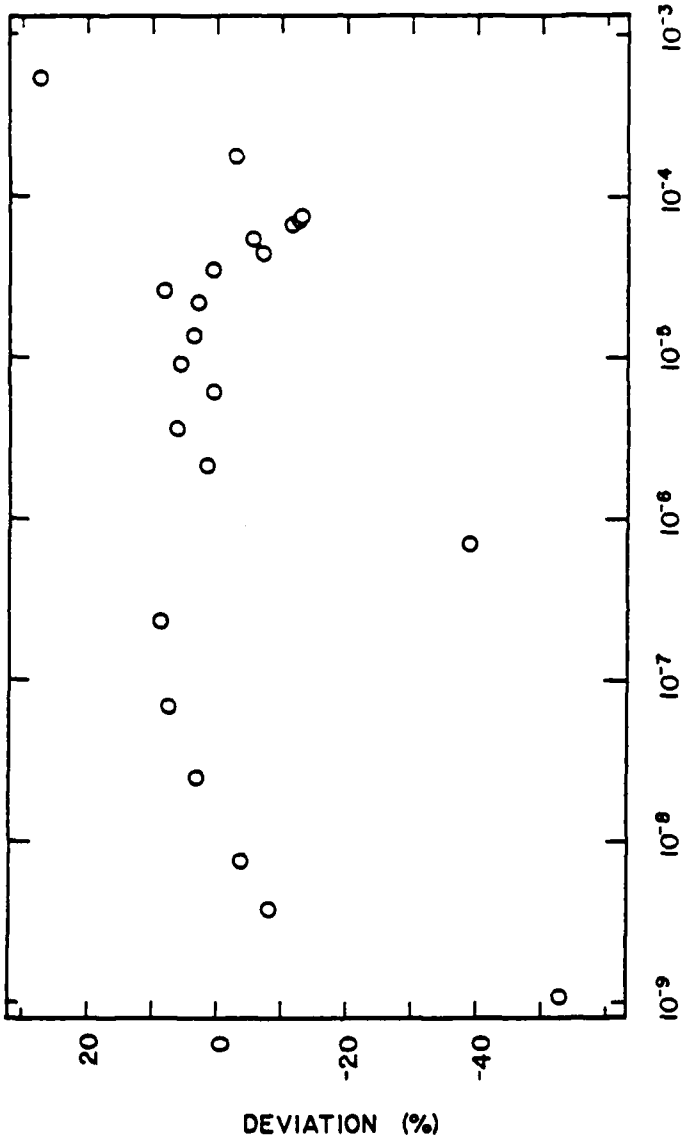

Figure 30 Measured deviation in $\mathcal{S}$.

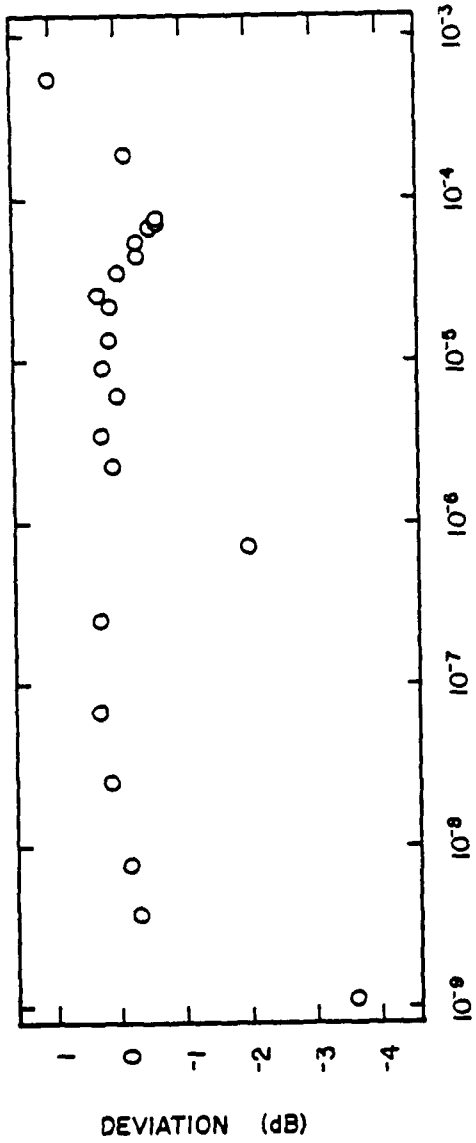

Figure 31 Measured deviation in dB.

summarized in Table 3. Variations here may be largely due to the varying quality of the cleave and the difficulty of using the neutral density filters.

4.4.3 Crosstalk

This parameter was very difficult to measure as it required optical isolation of one waveguide from an adjacent one. Once this condition was achieved, the measurement was still limited to about 30 dB due to the instrument sensitivity. Measurements at maximum power illumination did not reveal any response in the adjacent detectors due to crosstalk so it can be assumed to be better than 30 dB.

Table 3

Tracking of waveguide detector array

Detector Numbers	Laser Power Attenuation (dB)	Photoresponse Mean, M (ma)	Standard Deviation, δ (ma)	10 log $\frac{(M+\delta)}{M}$ (dB)
1 to 30	0	3.16	0.736	0.91
1 to 20	0	2.93	0.432	0.60
1 to 20	- 4.3	1.41	0.289	0.81
1 to 20	- 8.9	0.660	0.226	1.3
1 to 20	-13.2	0.414	0.126	1.2

5. CONCLUSIONS

The results of this evaluation are very promising. The waveguide photodiodes have shown a dynamic range of nearly 60 dB and possibly greater. This range is compatible with present CW laser emission levels for optimum coupling. The response characteristic is not logarithmic, but represents a good deal of compression compared to a linear response. Device uniformity is better than 15% (0.60 dB) for 20 devices. This is one area that can certainly be improved, since these were not exceptional devices. The measured crosstalk is quite reasonable, but should be examined more closely to be complete. The results of these measurements and analysis are summarized in Table 4. Fabrication of the array still remains the largest variable. The array with FETs has been shown to be a challenge to fabricate. However, the results are encouraging. The device layout and geometry seem to be good choices. The device processing, however, needs to be studied in more detail until the process is perfected. One possible change for the future would be to develop a planar structure in which isolation is provided by ion implantation, or by proton bombardment. Such a structure would not necessitate the thick photoresist layers necessary to cover the mesa. Subsequently linewidth control would improve, and resist edge profile could also be controlled.

Table 4

Summary of Evaluation

Power Range: 1.1 nwatt to 0.540 mwatt

Response Range: 1 μamp to 2.6 mamp

Dynamic Range: 57 dB

Response Linearity: ± 7%, (± 0.3 dB) from mean

maximum, + 26% (1.0 dB)

- 13% (0.6 dB)

Crosstalk: better than 30 dB between adjacent channels

Channel-to-channel Tracking:

30 adjacent detectors, 23% (0.91 dB)

20 adjacent detectors, 15% (0.60 dB)

The gate lift-off would have a much higher yield on a planar structure as well.

These results presented here support the continuation of work to fabricate the array with the mesa structure. Despite the drawbacks of the thick photoresist, fine linewidths can be obtained and lift-offs have been obtained before in similar structures. The waveguide and detector have been integrated with the good results shown previously. All that remains is the development of the correct procedure for the gate lift-off. With this development, the processing will be complete, and well defined structures can be fabricated.

6. BIBLIOGRAPHY

1. W.T. Lindley, R.J. Phelan, Jr., C.M. Wolfe, and A.G. Foyt, "GaAs Schottky Barrier Avalanche Photodiodes", *Applied Physics Letters* 14, 197, 1969.

2. G.E. Stillman, C.M. Wolfe, J.A. Rossi, and H. Heckscher, "Low-loss High Purity GaAs Waveguide for Monolithic Integrated Optical Circuits at GaAs Laser Wavelengths", *Applied Physics Letters* 28, 197, 1976.

3. C.E. Hurwitz, J.A. Rossi, J.J. Hsieh, and C.M. Wolfe, "Integrated GaAs-AlGaAs Double-Heterostructure Lasers", *Applied Physics Letters* 27, 241, 1975.

4. M.J. Sun, K.H. Nichols, W.S.C. Chang, R.O. Gregory, F.J. Rosenbaum, and C.M. Wolfe, "Gallium Arsenide Electroabsorption Avalanche Photodiode Waveguide Detectors", *Applied Optics* 17, 1568, 1978.

5. W. Franz, "Einflu Eines Elektrischen Feldes auf Eine Optische Absorptionskante", *Zeitschrift Naturforsch*, A 13, 494, 1958.

6. L.V. Keldysh, "The Effect of a Strong Electric Field on the Properties of Insulating Crystals", *Journal of Experimental and Theoretical Physics (USSR)* 34, 1138, 1958.

7. G.E. Stillman, C.M. Wolfe, J.A. Rossi, and J.L. Ryan, "GaAs Electroabsorption Avalanche Photodiodes", *Institute of Physics Conference Series* 24, Chapter 4, 1975.

8. D.B. Anderson, J.T. Boyd, M.C. Hamilton, and R.R. August, "An Integrated Optical Approach to the Fourier Transform", *IEEE Journal of Quantum Electronics*, QE-13, 4, 268, 1977.

9. G.E. Stillman, C.M. Wolfe, J.A. Rossi, and A.G. Foyt, "Unequal Electron and Hole Impact Ionization Coefficients in GaAs", *Applied Physics Letters* 24, 471, 1974.

10. K. Seeger, *Semiconductor Physics*, Springer-Verlag, New York, 1973.

11. D. Marcuse, *Theory of Dielectric Optical Waveguides*, Academic Press, New York, 1974.

12. R. Zuleeg and K. Lehovec, "High Frequency and Temperature Characteristics of GaAs Junction Field Effect Transistors in the Hot-Electron Range", *Institute of Physics Conference Series* 9, 240, 1970.

13. S.M. Sze, *Physics of Semiconductor Devices*, John Wiley, New York, 1969.